**NTNU – Trondheim**
Norwegian University of
Science and Technology

# A Bivariate Analysis of the Homogeneous Plane-Wave Assumption in Magnetotelluric Theory

**Jean-Michael Yves Poudroux**

Master of Science in Physics and Mathematics
Submission date: June 2015
Supervisor: Arne Brataas, IFY
Co-supervisor: Rune Mittet, EMGS

Norwegian University of Science and Technology
Department of Physics

# A Bivariate analysis of the homogeneous plane-wave assumption in Magnetotelluric Theory

## Applied on two Case Studies in the North Sea and Barents Sea

Jean-Michael Poudroux

**NTNU – Trondheim**
Norwegian University of
Science and Technology

Department of Physics

Faculty of Natural Sciences and Technology

Trondheim, June 2015

Jean-Michael Poudroux: *A bivariate analysis of the homogeneous plane-wave assumption in magnetotelluric theory: Applied on two Case Studies in the North Sea and Barents Sea*, June 2015

Supervisors:
Rune Mittet, EMGS
Vidar Markhus, EMGS
Arne Brataas, NTNU

Location:
Trondheim, Norway

# Abstract

The magnetotelluric method is an electromagnetic induction method used to image subsurface resistivity. It utilizes Earths' natural time-varying electromagnetic field as a source. The fields propagating into the subsurface are assumed to consist of homogeneous plane-waves. In a marine setting, the subsurface response is measured by a grid of receivers placed at the seabed. The homogeneous plane-wave assumption is a widespread and central argument for how traditional processing schemes are formulated and solved. In this thesis we provide a closer look on this assumption, by approximating the direct source field using up-down decomposition above the seabed. By organizing the data into receiver-pairs, we evaluate the homogeneous plane-wave assumption as a function of receiver-spacing. The method was applied on two offshore case studies located in the North Sea and Barents Sea. The results showed that the homogeneous plane-wave assumption was dependent on the receiver-spacings. The approximation was better for nearest neighbours, but decreased for receivers that were far apart.

"*Readers of Geophysics, as well as this writer, are mainly concerned with what is underneath their feet and are little interested in what goes on above their heads*" –
(Cagniard, 1953).

# Contents

# Chapter 1

# Introduction

## 1.1 Problem

The magnetotelluric (MT) method utilizes Earth's natural electromagnetic (EM) field to determine the electrical conductivity properties of the Earth (Cagniard, 1953; Tikhonov, 1950). The low frequency content, allows imaging at depths ranging from the upper oceanic crust to the mantle structure and deep tectonics. The essence of marine MT is to estimate the field impedance $\bar{\boldsymbol{Z}}$ of the sediments below the seabed. This is obtained by using simultaneous measurements of the horizontal electric and magnetic field components obtained from multiple measuring stations (receivers) positioned at the seabed. This method have been particularly useful in imaging large-scaled regions and high resistive structures such as salt- and basaltic-layers (Hoversten et al., 2000; Key et al., 2006; Panzner et al., 2014). The most fundamental assumption within this method is to model the EM fields as downward vertically propagating homogeneous plane-waves (Cagniard, 1953; Tikhonov, 1950). This assumption is commonly used in all modern MT processing schemes (Egbert, 2002). By modelling the fields as homogeneous plane-waves, one consequently assume a uniform current-sheet geometry for the source. However in reality the source geometry is much more complex, as the fields are generated by solar terrestrial interactions and global weather phenomena.

The focus of this thesis is however not with the subsurface. Instead we aim to provide a fresh view investigating the homogeneous plane-wave assumption by using up-down decomposition (Ursin, 1983; Amundsen et al., 2006) to approximate the direct source field above the seabed. There have not been, to the extent of the authors knowledge, studies done on the MT source field by using up-down decomposition. A common argument for the validity of the homogeneous plane-wave assumption is that the surveying scale is considerable smaller than the source scale (Dmitriev and Berdichevsky, 1979). Thus non-uniform events are not observable. Thus we propose to analyse the homogeneous plane-wave assumption, using the down-going fields, as a function of receiver-spacing. If the prerequisites for applying the homogeneous plane-wave assumption are invalid in the first place, one must

take source geometry into consideration and reformulate the problem accordingly.

The outline of this thesis is as follows. Chapter 2 provides a general introduction to the MT method. Chapter 3 gives a general description of how MT data is processed. Chapter 4 derives the method of how we analyse the homogeneous plane-wave assumption. Chapter 5 displays the results of applying the equations derived in Chapter 4 on two case studies, combined with a general discussion and concluding remarks.

# Chapter 2

# The Magnetotelluric Method

## 2.1 Natural Sources

The frequency band in MT studies can consist of both long-term and short-term variations ranging from $10^{-5}$ - $10^{4}$ Hz (Simpson and Bahr, 2004). The main driving mechanism for the low frequency fields are the interactions between solar wind plasma and the upper layers of Earth's atmosphere, specifically the magnetosphere and ionosphere (Vozoff, 1991).

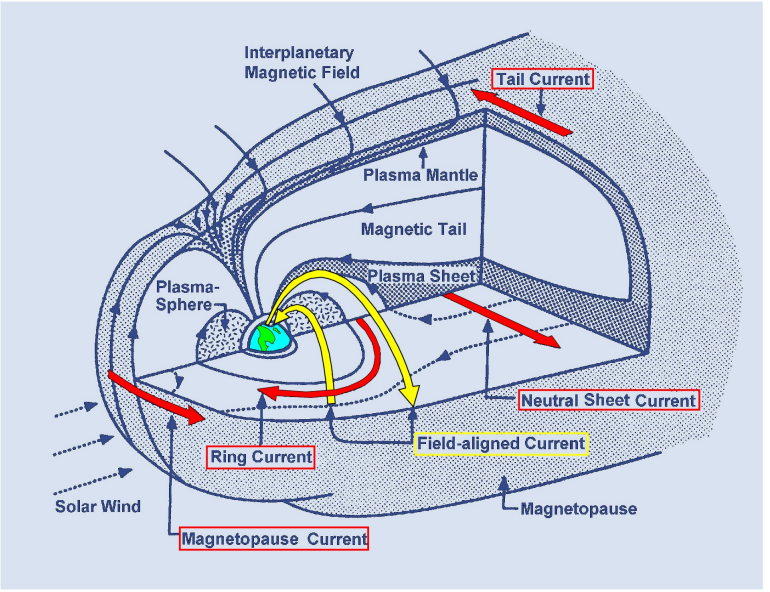


Figure 2.1: Illustration of the magnetosphere and the different atmospheric current systems (Kievelson and Russel, 1995).

The magnetosphere is defined as the region of space where charged particles are controlled by Earth's magnetic field (Figure 2.1). Within the inner edge of the magnetosphere resides the ionosphere. This layer is characterised by a high density of charged electrons and protons, with properties similar to an electrical insulator. Frequencies in the range $10^{-5}$ - $10^{-1}$ Hz are believed to be caused by excitation of the ionospheric layer (Vozoff, 1991). The excitations are caused by EM waves propagating within the magnetosphere. The vertical component of these fields do not penetrate the ionosphere. The transmitted fields form plane waves travelling down towards the Earth (Vozoff, 1991). The short-term fluctuations are caused by the global weather climate in the lower atmosphere. The background signal of global lightning storms can create EM waves oscillating in the range 10 - 50 Hz (also called Schumann resonances). The primary lightning signal make up the audiomagnetotelluric sources (1 Hz - 10 kHz). The transition between short-term and long-term variations is defined as the MT dead-band (0.1 - 10.0 Hz). The transition is usually characterised by poor data quality (Simpson and Bahr, 2004; Vozoff, 1991).

## 2.2 Source Disturbances

The high frequency content in particular regions is known to contain non-uniform source effects. Fluctuations in the ionosphere creates several different atmospheric currents illustrated in Figure 2.1. These currents can couple to the local magnetic environment creating numerous non-uniform events such as geomagnetic storms or irregular pulsations (Chave and Jones, 1987; Mareschal, 1986). Coupling of the Field-aligned currents in the auroral zone and coupling with the ring currents around the equator creates an EM rich environment known to induce non-uniform fields. Several authors have contributed with both numerical and theoretical methods on how to deal with non-uniformity in these particular regions (Hermance, 1978; Viljanen et al., 1999, 1993; Mareschal, 1986; Jones and Spratt, 2002; Carrasquilla and Rijo, 1998; Padilha, 1999). In terms of processing, the high energetic non-uniform events can create serious bias of the low frequency fields by spectral leakage (Prieto et al., 2007).

## 2.3 Historical Review

The simplicity of the current-sheet model, first proposed by Cagniard (1953), have been heavily debated over the years. Wait (1954) and Price (1962) stated that the relations between the inducing fields and the Earth, proposed by Cagniard, did not take into considerations the effects of varying vertical field components. Providing both theoretical and experimental arguments, the critiquing authors claimed that the MT method applicability was more restricted in terms of penetration depths than Cagniard had proposed. Madden and Nelson (1964) argued that the inconsistencies highlighted by Wait and Price could be explained by non-uniform source effects, but also and more importantly, the limitations of a plane-layered Earth-

model. Madden showed that the effects of finite horizontal wavelengths combined with non-horizontal conductivity structures did not restrict Cagniards' relations as stringent suggested by Price and Wait. However, the single-site data sampling strategy presented by Cagniard was recognized as insufficient to image the proper 3D response. Dmitriev and Berdichevsky (1979) provided a detailed theoretical analysis of the critique by Wait and Price. Their conclusions justified the applicability of the Cagniard-Tikhonov relations. In the following years, numerous contributions were made, providing both theoretical and experimental analysis of non-uniform source models. A further historical read can be found in the paper by Jones and Spratt (2002), which we will also quote Table 2.1 from.

Table 2.1: Source field theory for a 1-D layered Earth model (Jones and Spratt, 2002).

| Source field geometry | Reference |
|---|---|
| Uniform | Tikhonov (1950), Cagniard (1953) |
| Linear | Dmitriev and Berdichevsky (1979) |
| Wavenumber (repetitive in space) | Price (1962), Srivastava (1965) |
| Line Current | Hermance and Peltier (1970) |
| Arbitrary | Hibbs and Jones (1976a,b) |
| Dipole | Osipova et al. (1989) |
| 3D-Current System | Mareschal (1986),Viljanen et al. (1999, 1993) Pirjola (1998) |
| Moving Gaussian | Hermance (1978) |

## 2.4 Geophysical Exploration

The majority of the fields will be reflected due to the high resistivity contrast between air and the Earth. However, a small amount of the fields will transmit vertically (Dmitriev and Berdichevsky, 1979; Vozoff, 1972) into the subsurface sediments. The transmitted EM fields induces electrical currents within the Earth (telluric currents). Due to the skin-effect, the currents will create a pile-up of charge on the resistive boundaries, which in turn generate a secondary induced field propagating upwards. This secondary field carry the information of interest.

Although most rock-minerals below the seabed are considered electrical insulators, the pore space within resistivity rocks can be filled with conductive fluids. Sedimentary rocks filled with hydrocarbon (HC) can have several hundred times the resistivity compared to rocks filled with water-bearing sediments. In Table 2.2 we highlight typical resistivity values for sediments in the subsurface.

The potential of applying EM inductive methods to map Earth's conductive properties was early recognized due to the intrinsic high resistivity contrasts found within subsurface sediments (Cagniard, 1953; Tikhonov, 1950). However, it was not until recently that usage of active sources, also known as Controlled-Source Electromagnetics (CSEM), was established as a successful commercial surveying

Table 2.2: Approximative resistivity values for typical medium found in a marine environment.

| Formation | $\log \rho$ ($\Omega$m) |
|---|---|
| Seawater | -1 |
| Air | 16 |
| Shale | 1 |
| Gas Hydrates | 1 - 2 |
| Sandstone | 1 - 2 |
| Volcanic Rocks | 2 - 4 |
| Salt | 2 - 3 |
| Basalt | 2 |
| Petroleum | 9 - 16 |

tool in HC prospecting (Eidsmo et al., 2002). Note that CSEM is not new concept as it has been around since the 1960s. For a historical review we refer to the article by Constable (2010). In the next section we will explain the main components in conducting CSEM and MT surveying in a marine environment.

### 2.4.1 CSEM & MT Surveying

A typical CSEM survey consist of an surveying vessel towing a horizontal electric dipole (HED) above an array of sea-floor receivers (Figure 2.2). The survey layout depends on both complexity of bathymetry and desired data resolution. Receivers might be placed in a single line or in a grid, consisting of typically 10 - 150 receivers with a receiver spacing between 1.0 - 5.0 km. The HED can provide a typical frequency output of 0.05 - 10.0 Hz. In order to image a subsurface response, the EM signals are required to travel from the source, interact with the target and reflect back again to the receivers. However, the EM fields experience attenuation within the conductive seawater and sediments. The degree of attenuation increases as a function of frequency. Typical imaging depths and CSEM sensitivity are discussed by Mittet and Morten (2012).

The MT signal can be acquired alongside in a CSEM data gathering process. This occur in situations where the source is inactive, for instance during receiver deployment and retrieval, or when the receivers are sufficiently away from the active source. The low MT frequencies however require longer listening times compared to CSEM, and regions with prominent source effects require even longer (Chave and Thomson, 2004). The higher frequencies, around 1 Hz and above, are usually filtered out, either by the conductive sea-water or reflection at the air-seawater interface. The active source in CSEM can produce several different EM modes within the subsurface, but MT is dominated by vertically propagating waves. This makes CSEM sensitive in both horizontal and vertical resistivity, while MT can only image horizontal resistivity. However, the MT fields have a larger penetration depth due to the low frequency content. Therefore, CSEM is primarily used to

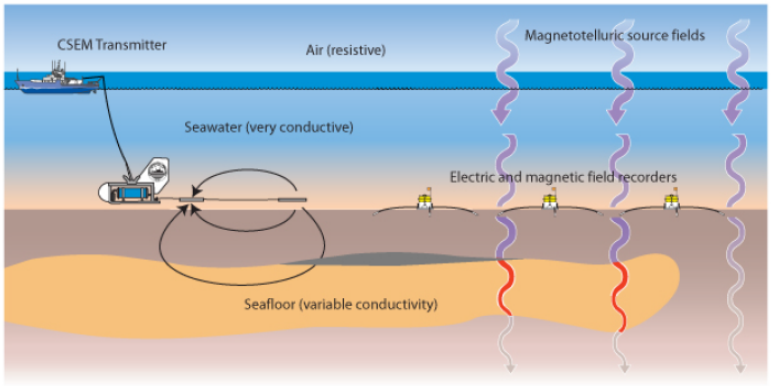


Figure 2.2: Illustration of the CSEM (left) and MT (right) system (Scripps Institute of Oceanography).

detect thin and shallow buried HC-reservoirs, while MT is used to image thick resistive structures, such as salt, basalt or volcanic rocks (MacGregor, 2003) or general large-region mapping. Therefore MT is often used as a complementary method alongside seismic and CSEM (Panzner et al., 2014; Kumar et al., 2014).

## 2.5 Magnetotelluric Theory

In this section we provide a general description of the relevant equations describing the behaviour of electromagnetic fields propagating in conductive mediums. We use the following set of temporal Fourier Transforms

$$\boldsymbol{F}(\omega) = \int_{-\infty}^{+\infty} \mathrm{d}t \boldsymbol{f}(t) e^{-i\omega t} \quad (2.5.1a) \qquad \boldsymbol{f}(t) = \int_{-\infty}^{+\infty} \mathrm{d}\omega \boldsymbol{F}(\omega) e^{+i\omega t}, \quad (2.5.1b)$$

where $i = \sqrt{-1}$, $t$ is time, $\omega = 2\pi f$ is the angular frequency, $\boldsymbol{f}(t)$ is a vector in space-time and $\boldsymbol{F}$ is the Fourier transformed space-time vector in the space-frequency domain.

### 2.5.1 Maxwell's Equations

The behaviour of the electromagnetic fields are in general described by Maxwell's Equations. Assuming a isotropic homogeneous medium, the Maxwells Equations in differential form are given as

$$\nabla \cdot \boldsymbol{D} = \rho_d \tag{2.5.2a}$$
$$\nabla \times \boldsymbol{E} = -\partial_t \boldsymbol{B} \tag{2.5.2b}$$
$$\nabla \cdot \boldsymbol{B} = 0 \tag{2.5.2c}$$
$$\nabla \times \boldsymbol{H} = \boldsymbol{J} + \partial_t \boldsymbol{D} \tag{2.5.2d}$$

where $\partial_t$ denotes the partial derivative with respect to time, $\boldsymbol{E}$ ($\mathrm{Vm}^{-1}$) and $\boldsymbol{B}$ (T) are respectively electric field and magnetic flux density, $\boldsymbol{D}$ ($\mathrm{Cm}^{-2}$) is the displacement field, $\boldsymbol{H}$ ($\mathrm{Am}^{-1}$) is the magnetic field, $\rho_d$ ($\mathrm{Cm}^{-3}$) is a charge density and $\boldsymbol{J}$ ($\mathrm{Am}^{-2}$) is a current-density vector. The relations between the displacement field and electric field, and magnetic flux density and magnetic fields are given by the linear constitutive relations

$$\boldsymbol{D} = \epsilon_0 \epsilon_r \boldsymbol{E} = \epsilon \boldsymbol{E} \tag{2.5.3a}$$
$$\boldsymbol{B} = \mu_0 \mu_r \boldsymbol{H} = \mu \boldsymbol{H} \tag{2.5.3b}$$

Where $\epsilon_0 = 8.85 \cdot 10^{-12}$ ($\mathrm{Fm}^{-1}$) and $\mu_0 = 4\pi \cdot 10^{-7}4$ ($\mathrm{Hm}^{-1}$) are physical constants identified as vacuum permittivity and vacuum permeability. The parameters $\epsilon_r$ and $\mu_r$ are denoted relative electric permittivity and relative magnetic permeability, and they are an intrinsic material dependent property. The majority of reservoir rocks and sediments are considered non-magnetic, therefore it is common to approximate $\mu_r \simeq 1.0$. The electric permittivity however, can vary over several orders of magnitude. The normal and parallel components of the electric and magnetic fields follow the corresponding boundary conditions between medium 1 and medium 2 characterised respectively with material properties $\epsilon_1, \mu_1$ and $\epsilon_2, \mu_2$,

$$\epsilon_2 \boldsymbol{E}_2^{\perp} - \epsilon_1 \boldsymbol{E}_1^{\perp} = \sigma_s \tag{2.5.4a}$$
$$\boldsymbol{E}_2^{\parallel} - \boldsymbol{E}_1^{\parallel} = 0 \tag{2.5.4b}$$
$$\mu_2 \boldsymbol{H}_2^{\perp} - \mu_1 \boldsymbol{H}_1^{\perp} = 0 \tag{2.5.4c}$$
$$\boldsymbol{H}_2^{\parallel} - \boldsymbol{H}_1^{\parallel} = \boldsymbol{K}_s. \tag{2.5.4d}$$

Here $\sigma_s$ ($\mathrm{Cm}^{-2}$) is a surface charge density and $\boldsymbol{K}_s$ ($\mathrm{Am}^{-2}$) is a surface current.

### 2.5.2 Conductivity

If we consider conductive mediums, one can rewrite the current density vector $\boldsymbol{J}$ in equation 2.5.2d, to consist of two terms $\boldsymbol{J} = \boldsymbol{J}_c + \boldsymbol{J}_0$. The first term on represents a conduction current. It is related to the electric field via Ohms law

$$\boldsymbol{J}_c = \sigma \boldsymbol{E}, \tag{2.5.5}$$

where the electric conductivity, $\sigma$ ($S\mathrm{m}^{-1}$), describes a materials ability to carry a current. It is also known by its reciprocal, resistivity, $\rho = 1/\sigma$ ($\Omega$m), which denotes the resistance of a current, and must not be mistaken for the charge density in equation 2.5.2a. The second term $\boldsymbol{J}_0$ is a current term not caused by induction. This can represent either the ionospheric current source or the active CSEM source.

### 2.5.3 Different Wave Equations

Electromagnetic fields propagating in conductive medium tend to attenuate diffusively. This means that the energy carried by the fields depletes into the surrounding medium, converting to heat. The second order partial differential equation governing this process is obtained by decoupling the electric and magnetic fields into a damped wave-equation using the constitutive relations and Ohm's law

$$\nabla^2 \boldsymbol{E} = \mu\sigma\partial_t \boldsymbol{E} + \epsilon\partial_t^2 \boldsymbol{E}. \tag{2.5.6}$$

The equivalent relation for the magnetic field is obtained by substituting $\boldsymbol{E} \to \boldsymbol{H}$. In deriving this equation we have assumed regions free of charge ($\rho = 0$) and currents ($\boldsymbol{J}_0 = 0$), with time-invariant material parameters. Applying the temporal Fourier transformation 2.5.1a on equation 2.5.7 yields

$$\nabla^2 \boldsymbol{E} = \mu\omega^2(i\sigma/\omega + \epsilon)\boldsymbol{E}. \tag{2.5.7}$$

Solutions to equation 2.5.7 are plane-waves of the form $\boldsymbol{E} = \boldsymbol{E}_0 e^{i\boldsymbol{k}\boldsymbol{x} - i\omega t}$, where $k = 2\pi/\lambda$ is the wave-number defined by the wavelength $\lambda$. Applying the solution ansatz to equation 2.5.7 yields a restriction on the magnitude of the wave-vector

$$k^2 = \omega^2\mu(i\sigma/\omega + \epsilon). \tag{2.5.8}$$

The plane-wave phase velocity is defined as the ratio between the angular frequency and wave-number

$$c \equiv \frac{\omega}{k}. \tag{2.5.9}$$

Since $k$ is a non-linear function of $\omega$, the phase-velocity will also be a function of $\omega$. Mediums that have phase-velocity dependent on angular frequency are called dispersive (Griffiths, 2008), and will cause the EM waves to diffuse. The diffusion behaviour enters via the conductive term. In non-conductive medium where $\sigma \simeq 0$, equation 2.5.6 is reduced to

$$\nabla^2 \boldsymbol{E} = c^{-2}\partial_t^2 \boldsymbol{E}, \tag{2.5.10}$$

which is a standard vector wave equation, with phase-velocity $c = \sqrt{1/\mu\epsilon}$, solely determined by the relative electric permittivity and relative permeability. Thus electromagnetic fields propagating in air ($\sigma_a \simeq 0$) experience negligible diffusion. However, within the conductive Earth (or seawater), the low frequency MT fields are primarily diffusive due to the quasi-static approximation (Vozoff, 1991)

$$\sigma \gg \epsilon\omega. \tag{2.5.11}$$

Neglecting the contributions from displacement currents compared to conductive currents, equation 2.5.6 reduces to a diffusion equation

$$\nabla^2 \boldsymbol{E} = D\partial_t \boldsymbol{E}, \tag{2.5.12}$$

with diffusion constant $D = \mu\sigma$. The dispersion-relation of the wave-number is reduced to

$$k \simeq \sqrt{\frac{\sigma\mu_0\omega}{2}}(1+i) = \kappa + i\kappa, \tag{2.5.13}$$

where we have used $\sqrt{i} = (1+i)/2$. Evaluating a plane-wave propagating in the $z$-direction within a conductive medium, we get

$$\boldsymbol{E} = \boldsymbol{E}_0 \cdot^{i\kappa(z-ct)} \cdot e^{-\kappa z}. \tag{2.5.14}$$

This EM wave travelling in the z-th direction will experience attenuation with a characteristic phase-velocity $c(\omega)$. The parameter, skin-depth, is as a characteristic length defined when the amplitude is attenuated a factor of $e^{-1}$. The skin-depth is conventionally used as a crude estimate for the penetration depth. The expressions for the skin-depth and phase-velocity in the quasi-static approximation are

$$\delta(\omega) = \sqrt{\frac{2}{\sigma\mu_0\omega}} \tag{2.5.15}$$

$$c(\omega) = \sqrt{\frac{2\omega}{\sigma\mu_0}}. \tag{2.5.16}$$

Incorporating Ohm's law and the quasi-static approximation into Maxwell's Equations, reveals the more familiar MT representation of equation 2.5.2d and 2.5.2b

$$\nabla \times \boldsymbol{E} = -\mu\partial_t \boldsymbol{H} \tag{2.5.17a}$$

$$\nabla \times \boldsymbol{H} = \mu\sigma\boldsymbol{E}. \tag{2.5.17b}$$

The rate of energy depleting into the conductive medium can be analysed by the energy current density vector, $\boldsymbol{S}$, also known as the Poynting vector. This vector represents the power flux, denoted as the amount of energy passing through a surface per time unit. The time-averaged Poynting vector of complex EM fields is defined as (Griffiths, 2008)

$$\langle \boldsymbol{S} \rangle = \frac{1}{2}\Re\{\boldsymbol{E} \times \boldsymbol{H}^*\}, \tag{2.5.18}$$

where the asterisk $*$ denotes the complex conjugate and $\Re$ is the real-operator.

### 2.5.4 Impedance

From equation 2.5.17a we observe that the presence of an external electric field generating a conduction current, will induce a magnetic field. Therefore it is of interest knowing the coupling strength between the magnetic field and electric field. Inferring the plane-wave solution ansatz to equation 2.5.17a yields the following relation

$$\boldsymbol{H} = \frac{1}{\mu_0\omega}(\boldsymbol{k} \times \boldsymbol{E}). \tag{2.5.19}$$

Assuming that $\boldsymbol{E}$ is polarized along x-axis and the wave-vector $\boldsymbol{k} = k\hat{z}$, where $k$ is evaluated in in a non-conductive medium we get

$$Z_{xy} = \frac{E_x}{H_y} = \frac{\mu_0\omega}{k} = \sqrt{-i\omega\mu_0\rho}. \tag{2.5.20}$$

This is known as the characteristic impedance related to a specific medium of resistivity $\rho$. In vacuum this is valued at $Z_0 = \sqrt{\mu_0/\epsilon_0} \simeq 385.0\ \Omega$. The resistivity and corresponding phase-lag between electric and magnetic fields are

$$\rho = \frac{1}{\mu_0 \omega}|Z_{xy}|^2 \qquad (2.5.21) \qquad \Phi = \mathrm{Arg}\left(Z_{xy}\right) = \frac{\pi}{4}. \qquad (2.5.22)$$

Assuming a 1D multiple layered conductivity model of the Earth, the total field impedance, $Z_{xy}$, defined as the ratio of the measured electric and magnetic field components, can be written as function of characteristic impedance in layer 1 plus contributions from multiple reflection beneath (See Figure 2.3).

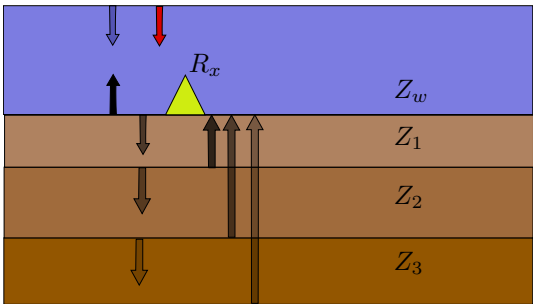


Figure 2.3: Up- and down-going field components registered by a receiver ($R_x$) placed at the seabed. The red arrow indicate direct MT source field, while the black arrows are up-/downgoing reflections.

The resulting field impedance registered by the receivers are given by a recursion formula Ward and Hohmann (1989)

$$\hat{Z}_i = Z_i \frac{\hat{Z}_{i+1} + Z_i \tanh(ik_i h_i)}{Z_i + \hat{Z}_{i+1} \tanh(ik_i h_i)} \qquad (2.5.23)$$

Here $h_i$ is the layer thickness and $Z_i$ is the characteristic impedance of layer $i$. For the respective high and low frequency limits we have $Z_{xy}(\omega) \simeq Z_1$ and $Z_{xy}(\omega) \simeq Z_3$. Incorporating the field impedance with equation 2.5.21, we obtain the apparent resistivity and associated impedance phase (Cagniard, 1953)

$$\rho_{xy}(\omega) = \frac{1}{\mu_0 \omega}|Z_{xy}(\omega)|^2 \qquad (2.5.24) \qquad \Phi_{xy}(\omega) = \mathrm{Arg}[Z_{xy}(\omega)]. \qquad (2.5.25)$$

Apparent resistivity provides an qualitative estimate of the horizontal resistivity as a function of depth. Both apparent resistivity and impedance phase are dispersion relations, varying smoothly as a function of $\omega$. The behaviour of the impedance phase can help predict the behaviour of the apparent resistivity (Weidelt, 1972). For higher dimensional models one must consider the effects of anisotropy and

source field polarization. Therefore a more general approach is given by the field impedance tensor

$$\begin{bmatrix} E_x \\ E_y \end{bmatrix} = \begin{bmatrix} Z_{xx} & Z_{xy} \\ Z_{yx} & Z_{yy} \end{bmatrix} \begin{bmatrix} H_x \\ H_y \end{bmatrix}. \tag{2.5.26}$$

In this form $\bar{\boldsymbol{Z}}$ is rotational invariant, thus independent of source polarization. Vozoff (1991) gives an description for the field impedance tensor elements in 1D-, 2D- and 3D-case.

### 2.5.5 Up-Down Decomposition

The primary interest in MT or CSEM surveying is to estimate the conductivity model of the subsurface. This information is located in the up-going (reflected) fields, induced via telluric currents within the subsurface. The receivers at the seabed record the total field, which consist of both up-going (U) and down-going (D) components. In CSEM one can get considerable contaminating contributions from the MT field or the air-wave in shallow waters (Nordskag and Amundsen, 2007; Mittet and Gabrielsen, 2013). To enhance the sensitivity of the up-going fields one can perform a local up-down decomposition (Ursin, 1983). Assuming vertically propagating waves, the up- and down-going field components are given (Amundsen et al., 2006)

$$E_x^D = \frac{1}{2}(E_x + Z_a H_y) \tag{2.5.27a}$$
$$E_y^D = \frac{1}{2}(E_y - Z_a H_x) \tag{2.5.27b}$$
$$E_x^U = \frac{1}{2}(E_x - Z_a H_y) \tag{2.5.27c}$$
$$E_y^U = \frac{1}{2}(E_y + Z_a H_x) \tag{2.5.27d}$$

$$H_x^D = \frac{1}{2}(H_x - Z_a^{-1} E_y) \tag{2.5.28a}$$
$$H_y^D = \frac{1}{2}(H_y + Z_a^{-1} E_x) \tag{2.5.28b}$$
$$H_x^D = \frac{1}{2}(H_x + Z_a^{-1} E_y) \tag{2.5.28c}$$
$$H_y^D = \frac{1}{2}(H_y - Z_a^{-1} E_x) \tag{2.5.28d}$$

where $Z_a$ is the characteristic impedance defined in equation 2.5.20. For the general 3D case we refer to the article by Amundsen et al. (2006).

# Chapter 3

# Magnetotelluric Data

## 3.1 Difficulties in Data Acquisition

The dynamic medium surrounding the receivers can generate significant amounts of motion noise. Movement of sea-water can induce local EM currents, or create instrumental vibrations, which are picked up by the receivers. Swells are known to produce noticeable motional receiver noise (Lezaeta et al., 2005). However, these effects are most prominent for the higher frequencies $\sim$ 1.0 Hz at water-depths less than 300 m. Tidal streams with a periodicity of 12.5 hours are also observable effects, but since the periodicity is known it is easy to accommodate for in processing. The bathymetry surrounding the receivers is also known to contaminate the signal (Key and Constable, 2010).

## 3.2 Time to Frequency Domain Transform

There are two main steps in the pre-processing routine. First step is to calibrate the electric and magnetic time-series for hardware characteristics such as induction-coil cross-talk, time drift, data imprints from the logger writing the data to memory and instrumental noise. The receivers used by EMGS' have approximately 2.0 ms drift for one week of MT data gathering. Figure 3.1 demonstrates the electromagnetic data before and after calibration.

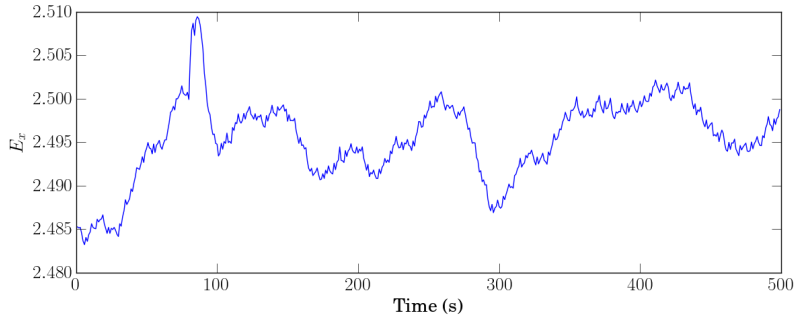


(a) Uncalibrated Raw data

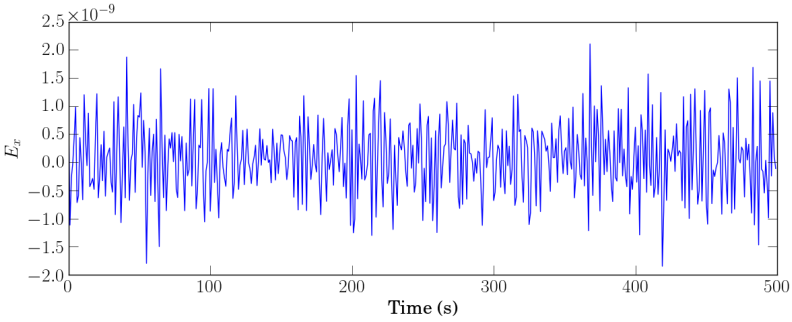


(b) After calibration in time-domain

Figure 3.1: Electromagnetic data before and after calibration. After calibration the electric MT field have sensible values $\sim 10^{-7}\ V/m$.

The next step is to transform the calibrated MT data to the frequency wave-domain. However, if the estimation of the Fourier spectrum is done via regular Fourier-transforms, the results are often biased due to spectral-leakage (Wei, 2006) as the variance of the estimator is independent of the sample size (Wei, 2006, chap. 13). This unsatisfactory property is often corrected by smoothing the time-series with a window function. In geophysical applications the multi-taper method developed by Thomson (1982) has been established as the superior method in terms of providing an unbiased estimate of the power-spectrum of a finite time-series. The Short-Time-Fourier Transform (STFT) on data sequence $x(t)$ can be written as,

$$x(\omega, \tau) = \sum_t w(t-\tau)x(t)e^{-i\omega t} \tag{3.2.1}$$

where $w(t)$ is the taper-function, $\omega$ is the angular frequency and $\tau$ is the ordering index. Conventionally a version of the orthogonal Slepian sequences (Thomson, 1982; Percival and Walden, 1993) are chosen for the taper function. The orthogonal tapers provide an low biased low spectrum leakage estimate of the Fourier-transformed sequence. For an extensive read about the method and other physical

applications, and for a description on how to implement the multi-taper method, the reader is referred to the literature; Percival and Walden (1993),Chave and Thomson (2004).

## 3.3 The Statistical Problem

In general the MT signal is non-stationary, and increasingly non-uniform for higher frequency content. The addition of sudden high-energetic MT bursts (hereby referred to as outliers) caused by non-uniform source phenomena, occurring non-periodically at seemingly random times creates a significant statistical problem. As mentioned by Chave and Jones (1987) there exist no realistic statistical method to detect outliers *a priori*. Any attempt on creating such methods increase in difficulty as the extreme data manifests differently in electric and magnetic field components for different receivers. There have been several different suggested methods in providing robust estimates of the impedance tensor. For instance, straight forward Least Squares minimizations and Remote Reference method (Gamble. et al., 1979) with different variations. However, these methods were unstable and gave biased results. A brief rendition of the given procedures can be found in Chave and Thomson (2004). Processing schemes following a Robust Multivariate Errors in Variables (RMEV) method has been established as the superior way of reducing the influence of outliers and providing robust estimates for the field impedance (Egbert, 1997, 2002; Jones et al., 1989; Chave and Thomson, 2004). The RMEV algorithm allows for noise in both electric and magnetic data, and uses data from multiple receiver data to enhance signal-to-noise ratios. However, this algorithm does not evaluate the plane-wave above the seabed like we propose to do. In conclusion the source effects consist of 3D non-stationary phenomenons with strong regional and periodically variations, which has been proven difficult to accurately model (Viljanen et al., 1993; Chave and Thomson, 2004).

### 3.3.1 Circularity

A common assumption in complex MT data is to assume circularity (Ollila et al., 2012). This means that both real and imaginary data are Gaussian-distributed and uncorrelated. Data that is heavily influenced by outliers, will distort the circularity as the tails of the real- and imaginary distributions can increase independently (Chave and Jones, 1987). However, if the data can be consider circular, then the marginal amplitude- and phase-distribution is well defined. Assuming circularity, will cause the amplitude to follow a Rayleigh distribution and the phase to be uniformly distributed on the interval $[-\pi, \pi]$. For additional information regarding the criteria of circularity and the distributions governing amplitude and phase, the reader is referred to the literature; Ollila et al. (2012); Chave and Lezaeta (2006); Chave et al. (1987). In Figure 3.2 we have plotted a scatter plot of the complex electric field. The plot demonstrates circularity.

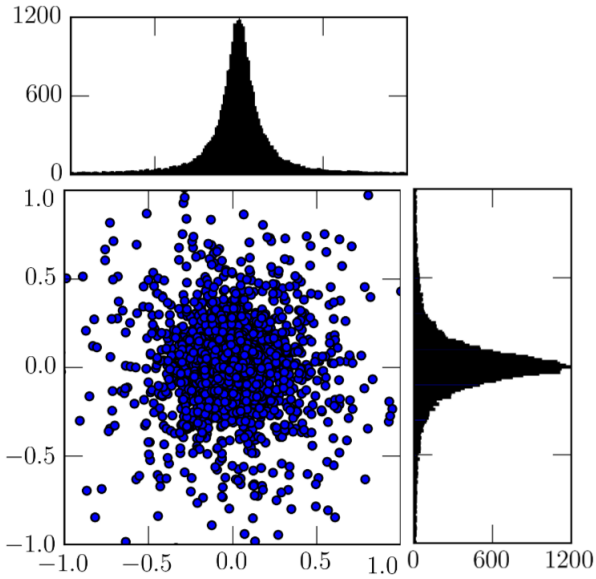


Figure 3.2: Complex scatter plot of the Fourier transformed MT data. Horizontal and vertical axis are respectively real and imaginary axis, with included distributions of real-(top) and imaginary-components (right).

## 3.4 Inversion

Provided one have multiple simultaneous recordings of the horizontal electric- and magnetic field components one can solve equation 2.5.26 an obtain an estimate for the field impedance. A common approach is to pose the problem as an inversion problem (Hohmann and Raiche, 1988). The problem then becomes to recreate the measured field response from a modelled impedance estimate. The inverse transform is given by Maxwell Equations. Further one reformulate the inversion problem, to a minimization problem. The cost function is defined as the difference between observed impedance, $Z^{obs}$, and modelled impedance, $Z^n$. The modelled impedance is improved iteratively until it reaches an acceptable convergence level (if it converges). The minimization function, also known as the misfit function, can be defined as (de la Kethulle de Ryhove and Mittet, 2014), with simplified notation

$$\psi^n = \sum W|Z^{obs} - Z^n|^2 + \psi_{reg}, . \tag{3.4.1}$$

The summation is done over all relevant parameters (cartesian coordinate, angular frequency, receiver position vector). The superscript $n$ corresponds to the iteration number. The kernel is weighted by $W$, which is normally chosen as a function of the standard deviation of the observed data. The last term on the right-hand side is a regularization term. This ensure that the estimated conductivity structure does not violate geological and physical principles. To showcase the output of a full MT

processing scheme we include the 3D MT inversion results from de la Kethulle de Ryhove and Mittet (2014). Figure 3.3 shows two cross-sections of the subsurface resistivity structure. Three resistive objects were identified by the inversion.

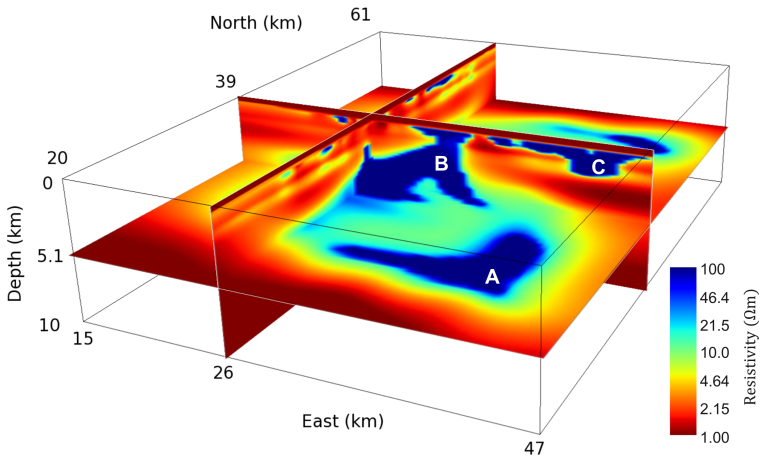


Figure 3.3: Both vertical and horizontal cross-sections of the resistivity structure obtained from a full 3D MT inversion (de la Kethulle de Ryhove and Mittet, 2014). Object $A$ and $B$, indicated by blue, was identified as salt structures. $A$ was estimated to be 1 km thick, and $B$ was estimated to maximum thickness of 5.5 km. Object $C$ in the background was interpreted as a shallow resistive structure which was also confirmed in a separate CSEM inversion.

# Chapter 4

# Analysing the Plane-wave

## 4.1 Preparing Data

In this project we have used EMGS' automated pre-processing schemes to calibrate and transform the electric and magnetic data in the time-domain to the complex frequency-space domain. The STFT is based on a version of the multitaper method. In the following we assume that the estimated electric and magnetic spectral coefficients exhibit circularity with a low bias and low spectral leakage. The data is obtained from $r = 1, ..., R$ receivers, each with $N$ electric and magnetic $E_i(\boldsymbol{\xi}_r, \omega, \tau)$ and $H_i(\boldsymbol{\xi}_r, \omega, \tau)$ measurements. The $i$ refers to $x$ and $y$ field components, $\boldsymbol{\xi}_r = [x_r, y_r, z_r]$ is the receiver position vector, $\omega$ is the angular frequency and $\tau$ is the Fourier-transform index variable. The vertical plane is spanned by the x- and y-axis, while the positive z-axis is defined downward into the subsurface. To analyse the homogeneous plane-wave assumption we transform each receiver data in three steps explained in the following sections.

### 4.1.1 Rotation

First all receiver field-components are aligned. The electric and magnetic fields are rotated for each receiver so that $E_{x,r}$ and $H_{x,r}$ points towards the geographical North, and $E_{y,r}$ and $H_{y,r}$ points towards the geographical East. Note that this choice is arbitrary, and the direct source field can be polarized in any direction. The rotation angle, $\Phi_r$, required to align the fields is unique for each receiver. This is due to the free fall during receiver deployment. The rotated electric and magnetic fields $E'_{i,r}$ and $H'_{i,r}$ are obtained by $\boldsymbol{E}'_r = \boldsymbol{R}_r \boldsymbol{E}_r$ and $\boldsymbol{H}' = \boldsymbol{R}_r \boldsymbol{H}$ where $\boldsymbol{R}_r$ is the associated rotation matrix for receiver $r$

$$\boldsymbol{R}_r = \begin{bmatrix} \cos(\Phi_r) & -\sin(\Phi_r) \\ \sin(\Phi_r) & \cos(\Phi_r) \end{bmatrix}. \tag{4.1.1}$$

### 4.1.2 Extract Down-going Source Field

The up-down decomposition scheme is conventionally used to enhance the subsurface sensitivity by reducing the influences of the down-going fields (Amundsen et al., 2006). However, we propose to do the opposite. By extracting the down-going field with an up-down decomposition above the seabed, we aim to reduce the influence from the inhomogeneous subsurface response. However, the down-going field components in MT can have multiple contributions, different from the direct source field. These contributions are secondary reflections from the water-air interface, and guided fields from surrounding bathymetry and coastal-effects (Key and Constable, 2010). However if we have a plane subsurface geometry, and sufficiently large water-depths, these two contributions are negligible. Thus the down-going fields are now an approximation of the direct source field. By following the derivations as in Chapter 2.5.5 we obtain the down-going fields. Note that equation 2.5.20 indicate that the down-going electric and magnetic fields contain equivalent information. Hence we only extract the electric down-going field

$$E_x^D(\boldsymbol{\xi}_r, \omega, \tau_m) = \frac{1}{2}(E'_x(\boldsymbol{\xi}_r, \omega, \tau_m) + Z_w(\omega)H'_y(\boldsymbol{\xi}_r, \omega, \tau_m)) \tag{4.1.2a}$$

$$E_y^D(\boldsymbol{\xi}_r, \omega, \tau_m) = \frac{1}{2}(E'_y(\boldsymbol{\xi}_r, \omega, \tau_m) - Z_w(\omega)H'_x(\boldsymbol{\xi}_r, \omega, \tau_m)). \tag{4.1.2b}$$

Where $Z_w(\omega)$ is the characteristic impedance of sea-water calculated in accordance with equation 2.5.20. As mentioned by Amundsen et al. (2006), the common practice is to assume a 1D formalism, approximating the EM fields to propagate vertically with little lateral variations. Still, under this assumption, Amundsen et al. (2006) is able to show significantly increased sensitivity to both synthetic and real data when performing up-down decomposition. Thus we use the down-going field as an approximation.

### 4.1.3 Redatuming

As the receivers are placed on an uneven sea-bed, the down-going field recorded by each receiver will differ due to the field attenuation in the conductive seawater. To accommodate this, we redatum the fields for each receiver from position $\boldsymbol{\xi}_r = [x_r, y_r, z_r]$ to $\boldsymbol{x}_r = [x_r, y_r, z_b]$, where $z_b$ is chosen as the minimum value of all receiver z-positions $z_b = min(\{z_r\})$. For the down-going fields, the correction term will consist of an amplitude gain and a negative phase shift. The corrections are given by $\kappa$ in equation 2.5.13, and the redatumed electric fields for receiver $r$ are then given by

$$E_{i,r}(\boldsymbol{x}_r, \omega, \tau) = E_{i,r}^D(\boldsymbol{\xi}, \omega, \tau) \cdot e^{+\kappa(\omega)(\boldsymbol{x}_r \cdot \hat{z}(1-i)} \tag{4.1.3}$$

with $\boldsymbol{x}_r = \boldsymbol{\xi} - z_b\hat{z}$. In Table 4.1 we list the correction terms for amplitude and phase for different frequencies for a 10.0 redatuming length. For frequencies $\sim 0.1$ Hz the correction terms are negligible.

Table 4.1: Amplitude and phase-corrections for different frequencies at $\Delta z = 10.0$ m.

| $f$ (Hz) | $\exp[-\Delta z_r/\delta(f)]$ (%) | $\Delta z_r/\delta(f)$ (°) |
|---|---|---|
| 10.0 | 90.4 | 6.44 |
| 1.0 | 96.5 | 2.04 |
| 0.1 | 98.9 | 0.64 |
| 0.01 | 99.9 | 0.06 |
| 0.001 | 99.9 | 0.02 |

### 4.1.4 Screening

Analysing the homogeneous plane-wave assumption require that we compare simultaneous measurements of the electric and magnetic fields. Therefore to assure all receiver measurements contain allowed measurements simultaneously, each receiver is passed through a screening algorithm. The procedure is as follows. First we check that the electric and magnetic field magnitude are above the suggested noise-levels (EMGS)

$$|E_i(\boldsymbol{\xi}_r, \omega, \tau_m)| < N_E = 3.0 \cdot 10^{-11} \text{ (V/m)} \tag{4.1.4a}$$
$$|H_i(\boldsymbol{\xi}_r, \omega, \tau_m)| < N_H = 5.0 \cdot 10^{-8} \text{ (A/m)}. \tag{4.1.4b}$$

Each $\tau_m$ that violate these inequalities are stored in respective demodulated time-arrays labelled, $\tau_r^N$, where upper index N refers to 'noise'. In addition to this, we also implement two supplementary criteria dedicated on checking for non-physical measurements. The first is denoted as the quotient-screening referred to by symbol $Q$,

$$Q_{E_i}(\boldsymbol{\xi}_r, \omega, \tau_m) = \frac{|E_i^D(\boldsymbol{\xi}_r, \omega, \tau_m)|}{|E_i^U(\boldsymbol{\xi}_r, \omega, \tau_m)|} < 1.0. \tag{4.1.5}$$

Here $D/U$ corresponds to respective down-going and up-going fields obtained by up-down decomposition locally at each receiver at the seabed. The down-going fields are expressed in equations 4.1.2a - 4.1.2b and the up-going fields are given as

$$E_x^U(\boldsymbol{\xi}_r, \omega, \tau_m) = \frac{1}{2}(E_x(\boldsymbol{\xi}_r, \omega, \tau_m) - Z_w(\omega) H_y(\boldsymbol{\xi}_r, \omega, \tau_m)) \tag{4.1.6a}$$
$$E_y^U(\boldsymbol{\xi}_r, \omega, \tau_m) = \frac{1}{2}(E_y(\boldsymbol{\xi}_r, \omega, \tau_m) + Z_w(\omega) H_x(\boldsymbol{\xi}_r, \omega, \tau_m)). \tag{4.1.6b}$$

The Q-ratio criteria demands that above the seabed, the MT field should dominate preferred to the subsurface response. However this assumes that we have a flat seabed to ensure we are not influenced by coast-effects (Key and Constable, 2010). If the seabed is uneven the down-going field can propagate downward and be guided by the seabed, and then reflect up again without being transmitted downwards. The second criteria is targeted at the energy conservation. Here we require that the vertical component of the Poynting vector is positive, effectively pointing into the subsurface

$$S_z(\boldsymbol{\xi}_r, \omega, \tau_m) = \frac{1}{2\mu_0} \Re[\boldsymbol{E}(\boldsymbol{\xi}_r, \omega, \tau_m) \times \boldsymbol{H}^*(\boldsymbol{\xi}_r, \omega, \tau_m)]_z > 0.0. \tag{4.1.7}$$

The Poynting vector is calculated using the total fields recorded at the seabed. If $S_z$ points upward then the Earth is producing energy, which is physically not allowed. Note that both equation 4.1.5 and 4.1.7 are evaluated at the seabed. Again these screening times gets stored to associated screening arrays in $\tau_r^Q$ and $\tau_r^S$. The total screening array for receiver $r$ is then the union of all the different screening arrays

$$\tau_r^T = \tau_r^N \cup \tau_r^Q \cup \tau_r^S. \tag{4.1.8}$$

As each receiver is passed through these screening criteria we generate one $\tau_r^T$ for each. Subsequently to analyse the entire survey, we create the total screening array $\mathcal{T}$

$$\mathcal{T} = \tau_1^T \cup \tau_2^T ... \cup \tau_R^T. \tag{4.1.9}$$

We note that this is a very strict criteria, strongly dependent on the number of receivers $R$. However it is necessary to have comparable measurements between receivers for each $\tau_m$. The data that has passed through these filters will be referred to as 'screened' data denoted by the calligraphic font $\mathcal{E}$. We include both screened and unscreened data in our analysis.

## 4.2 Notation

At this point we will simplify the complex field notation, as we are analysing amplitude and phase separately. The complex redatumed down-going electric field $E_i(\boldsymbol{x}_r, \omega, \tau)$ are separated into associated amplitude $A_i(\boldsymbol{x}_r, \omega, \tau)$ and phase $\phi_i(\boldsymbol{x}_r, \omega, \tau)$ as such

$$E_{i,r} = A_{i,r} \cdot e^{\phi_{i,r}}. \tag{4.2.1}$$

The $i$ refers to the $x$ and $y$ electric field components and the function arguments are written in short $A_{i,r} = A_i(\boldsymbol{x}_r, \omega, \tau)$ and $\phi_{i,r} = \phi_i(\boldsymbol{x}_r, \omega, \tau)$. The receiver index $r$ is either given by a subscript with the amplitude, $A_{i,r}$, or inside on the position vector $\boldsymbol{x}_r$. The usage of symbol $D$ indicating down-going field have been omitted. Any subsequent reference to either $A$ or $\phi$ implicitly means the re-datumed down-going field.

## 4.3 Bivariate Analysis

The homogeneous plane-wave assumption is analysed by examining the statistical relation-ships between simultaneous amplitude- and phase-measurements of the redatumed down-going electric MT field for multiple receiver-pairs $\{r, q\}$

$$A_i(\boldsymbol{x}_r, \omega, \tau) = A_i(\boldsymbol{x}_q, \omega, \tau) \tag{4.3.1a}$$

$$\phi_i(\boldsymbol{x}_r, \omega, \tau) = \phi_i(\boldsymbol{x}_q, \omega, \tau). \tag{4.3.1b}$$

We aim to analyse how well the assumption is fulfilled for different receiver-spacings $|\boldsymbol{x}_r - \boldsymbol{x}_q|$ and different frequencies $f = \omega/2\pi$. This is done by organizing the receivers in the following manner. Each possible receiver-pair combination $\{r, q\}$ are binned into groups, $g_t$, characterised by a receiver-spacing $\delta_t$. Only unique pairs are allowed into each group. This means that receiver-pairs $\{1, 2\}$ and $\{2, 1\}$ is equivalent. We evaluate all pairs within each group by four "goodness of fit" tests. Both receivers are valued on an equal footing within each receiver-pair, therefore the tests are required to be symmetric in $r$ and $q$. The average fitness of group $g_t$ will indicate how well the given dataset of frequency $f$ can be represented with the homogeneous plane-wave assumption at the corresponding receiver-spacing $\delta_t$. The first two tests are done with the correlation function on amplitude- and phase-measurements between receiver-pairs. The next texts aim to quantify the difference in amplitude- and phase-measurements between receivers $\{r, q\}$ by scaled residuals. The scaling is chosen so that the fitness values are bounded between zero and unity. The following sections deduces the receiver-pair tests, but first we give a brief review of the correlation function.

## 4.4 Correlation Function

The correlation function between two data-sets $x = \sum_i x_i$ and $y = \sum_i y_i$ can be defined as (Wei, 2006)

$$C(x, y) = \frac{E[(x - E[x])(y - E[y]))}{\sigma_x \sigma_y} \tag{4.4.1}$$

where $E[-]$ is the mean operator, and $\sigma$ is the standard deviation. The correlation function is symmetric in data input $C(x, y) = C(y, x)$. The output of this function is a correlation factor valued between -1.0 and +1.0, indicating the linear relationship between $x$ and $y$. A positive degree of correlation suggests that the curves follow each other, while a negative trend suggest that they separate. Different degrees of correlation is illustrated in Figure 4.1

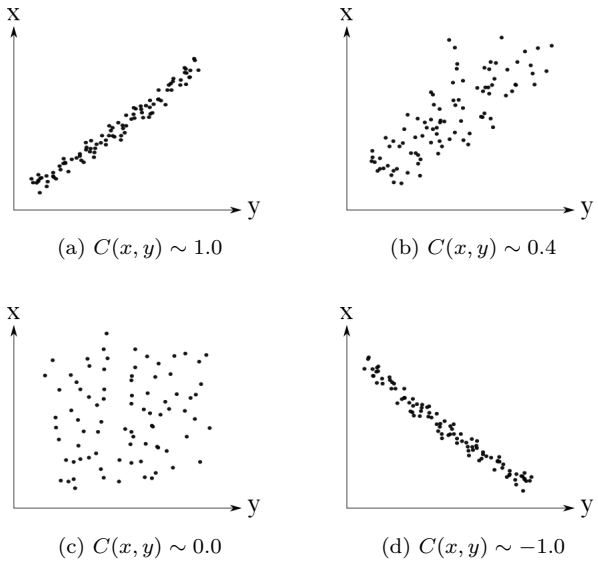


(a) $C(x, y) \sim 1.0$ (b) $C(x, y) \sim 0.4$

(c) $C(x, y) \sim 0.0$ (d) $C(x, y) \sim -1.0$

Figure 4.1: Illustrations showcasing the degree of correlation with the data.

For finite data samples we use the sample estimators for the mean and standard deviation, thus we get the sample correlation function

$$\hat{C}(x, y) = \frac{\sum_j^N (x_j - \bar{x}) \cdot (y_j - \bar{y})}{\sqrt{\sum_j^N (x_j - \bar{x})^2} \sqrt{\sum_j^N (y_j - \bar{y})^2}}. \tag{4.4.2}$$

For a constant $b$ we note the following multiplicative and additive properties of the correlation function $C(x, bx) = 1.0$, $C(x, y + b) = C(x, y)$. Thus the correlation function is insensitive when comparing the magnitude of the two data-sets, and if they have a constant difference in the mean. This means that in terms of describing amplitude homogeneity or phase-differences, the correlation function is a poor choice. Nonetheless, the correlation function will provide an insight whether there exist a linear relationship between the variables, which there should be according to the homogeneous plane-wave assumption.

## 4.5 Homogeneous Plane-Wave Tests

### 4.5.1 Amplitude

The amplitude can be significantly influenced by outliers. This will effectively bias the estimate of the mean, if one uses the standard sample mean estimator. In datasets that are heavily affected by outliers, the median operator is usually applied to estimate the mean instead. In addition if the outliers are occurring in

patches, this might create non-stationary phenomenon in the amplitude variance. A prerequisite for calculating the sample correlation function is that both series are stationary in mean and variance (Wei, 2006). However, in our approach we have no way of identifying such outliers. In fact outliers may very well be a manifestation of the inhomogeneous MT source. Hence we rely on the standard sample mean estimator. The sample amplitude-correlation function between receiver $r$ and $q$ is thus defined as

$$C_i^A(A_{i,r}, A_{i,q}) = \frac{\sum_{\tau_j}[A_{i,r}(\tau_j) - \langle A_{i,r}(\tau)\rangle_\tau][A_{i,q}(\tau_j) - \langle A_{i,q}(\tau)\rangle_\tau]}{\sqrt{\sum_{\tau_j}[(A_{i,r}(\tau_j) - \langle A_{i,r}(\tau)\rangle_\tau)]^2 \sum_{\tau_k}[(A_{i,q}(\tau_k) - \langle A_{i,q}(\tau)\rangle_\tau)]^2}}. \tag{4.5.1}$$

Here we use the bracket symbols $\langle - \rangle$ to denote an average in $\tau$. To examine amplitude homogeneity we suggest the following parameter, $\alpha$, denoted as *amplitude ratio*

$$\alpha_{E_i}(A_{i,r}, A_{i,r}) = 1.0 - \left\langle \frac{|A_{i,r} - A_{i,q}|}{A_{i,r} + A_{i,q}} \right\rangle_\tau. \tag{4.5.2}$$

Equation 4.5.2 provides an estimate for difference in homogeneity between receiver-pair $\{r, q\}$ for a given angular frequency $\omega$ averaged over demodulated time $\tau$. It is symmetric in receiver-pairs and bounded between zero and unity. If $A_r = A_q$ then $\alpha = 1.0$, which implies perfect homogeneity. In the inhomogeneity limit $A_r \gg A_q$ then $\alpha \to 0$. The numerator within the bracket-term can be interpreted as a folded residual, $\varepsilon_{rq} = |A_r - A_q|$, which is weighted by the sum of the amplitudes at that given $\tau$. This results in a normalized residual $\tilde{\varepsilon}_{rq} = \varepsilon_{rq}/(A_r + A_q)$. This weighting increases sensitivity to amplitude measurements close to the paired mean amplitudes $\langle A_r + A_q\rangle_\tau$. In terms of describing how $\alpha$ behaves with $A_r$ and $A_q$ we introduce the ratio parameter $\gamma = \frac{A_{i,r}}{A_{i,q}}$ to equation 4.5.2

$$\alpha_{E_i}(\gamma) = 1.0 - \left\langle \frac{|1.0 - \gamma|}{1.0 + \gamma} \right\rangle_\tau. \tag{4.5.3}$$

Amplitude homogeneity requires that $\gamma$ approaches unity. Averaging this ratio-parameter provides insight if it is approaching unity, but not from which direction. This lack of sensitivity is intrinsic to our bivariate approach. However, there may be a constant $a_0$ or higher order terms contributing to our test$\gamma' = \gamma + a_0 + A_q^{-1} + \gamma_2 A_q + .. + \gamma_n A_q^{n-1}$, where the $\gamma_{n+1}$'s carry appropriate dimensionality $[\gamma_{n+1}] = [A_q]^{-n}$. However any non-linear or constant terms will only appear in $\alpha$ as a deviation from the amplitude homogeneity.

### 4.5.2 Phase

Compared to the amplitude, analysing phase-variations between receivers is not that trivial. The phase of a complex number is uniquely defined between principal values, commonly in $[-\pi, \pi]$ or $[0, 2\pi]$. This phenomenon is known as phase-wrapping and is a classic signal processing problem. The unwrapped phase of the

down-going redatumed electric field for receiver $r$ can be written as

$$\phi_{i,r} = \psi_{i,r} + 2\pi \cdot n_{i,r} + \epsilon_{i,r} \tag{4.5.4}$$

Here $n_{i,r} \in \mathbb{Z}$ is the unwrapping-function, $\psi_i$ is the unwrapped phase and $\epsilon_{i,r}$ is a noise term. The noise $\epsilon_{i,r}$ can add additional wrapping. Phases $\psi_{i,r}$ close to $\pm\pi$ that experience a sufficiently large noise-term, $\epsilon_{i,r}$, can cause the phase to fold back to $\mp\pi$. In Figure 4.2 we highlight the noise wrapping effects, and how they contribute falsely to the correlation function.

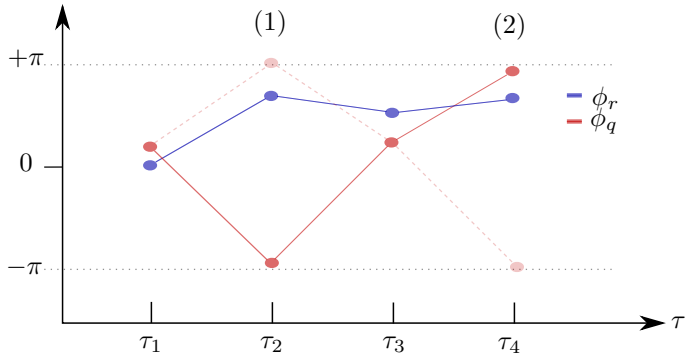


Figure 4.2: Two phase-curves indicated by red and blue. The dotted red line illustrates the true phase, unaffected by noise, while the solid line is the phase with noise-wrapping. There are two wrapping events occuring; first at $\tau_2$ second at $\tau_4$.

The correlation function will evaluate event (1) in Figure 4.2 as a false-negative contribution, adding a negative contribution which should be positive, while event (2) a false-positive, adding a positive contribution which should be negative. As a plane-wave signal is expected to correlate, event (1) should occur more frequently. Also for a plane-wave signal, the wrapping functions should be equal $n_{i,r} = n_{i,q}$ for all $\{r, q\}$. However the wrapping occurs, the process of unwrapping is a generally an ill-posed problem, and cannot be solved without additional information. Thus we present the correlation function of the unwrapped phase indicated by superscript $P$,

$$C_i^P(\phi_{i,r}, \phi_{i,q}) = \frac{\sum_{\tau_j}[\phi_{i,r}(\tau_j) - \langle\phi_{i,r}(\tau)\rangle_\tau][\phi_{i,q}(\tau_j) - \langle\phi_{i,q}(\tau)\rangle_\tau]}{\sqrt{\sum_{\tau_j}[(\phi_{i,r}(\tau_j) - \langle\phi_{i,r}(\tau)\rangle_\tau)]^2 \sum_{\tau_k}[(\phi_{i,q}(\tau_k) - \langle\phi_{i,q}(\tau)\rangle_\tau)]^2}}. \tag{4.5.5}$$

Keeping in mind that the false contributions to the correlation function may be skewed towards type (1) events, which makes this expression act as a lower threshold for the true correlation.

The last test is dedicated to analyse phase-residuals. Any non-zero phase-difference will indicate deviations from a plane-wave model. To analyse phase-differences we use equation 4.5.4 with simplified notation

$$\phi_{i,r} - \phi_{i,q} = \psi_{i,r} - \psi_{i,q} + 2\pi(n_{i,r} - n_{i,q}) + \epsilon_{i,r} - \epsilon_{i,q}. \tag{4.5.6}$$

The expression above for the phase-difference is valued between $[-2\pi, 2\pi]$. However, because of phase-wrapping, we can only evaluate the minimum angle of $|\phi_{i,r}-\phi_{i,q}|$ and $2\pi-|\phi_{i,r}-\phi_{i,q}|$. Instead of calculating the minimum phase-difference angle, we present a cosine-transform $\cos(|\phi_{i,q} - \phi_{i,q}|) = \cos(2\pi - |\phi_{i,q} - \phi_{i,q}|)$. This omits the wrapping contributions and the sign dependency. By using the trigonometric relation $\cos(x) = \sqrt{1/2 - \sin^2(x/2)}$, we re-normalize the cosine-transform and get the *associated phase-difference*,

$$\beta_{E_i}(\phi_{i,r} - \phi_{i,q}) = \left\langle \sin^2\left(\frac{\phi_{i,r} - \phi_{i,q}}{2}\right)\right\rangle_\tau. \tag{4.5.7}$$

This expression is symmetric in $r \leftrightarrow q$, and bound between zero and unity. The value of $\beta$ indicate the degree of fitness between the pairs.

## 4.6 Bivariate Averaging

After all receiver-pair compatibility tests have been deduced and discussed, we are ready to put the tests in their final format. The amplitude- and phase-correlation, amplitude ratio and associated phase-difference are evaluated on each receiver-pair within each group $g_t$ for a given frequency $\omega$

$$\bar{\mathcal{C}}^A_{E_i}(g_t, \omega) = \frac{1}{K_t}\sum_{\{r,q\}\in g_t} C^A_i(A_{i,r}, A_{i,q}, \omega) \tag{4.6.1a}$$

$$\bar{\mathcal{C}}^P_{E_i}(g_t, \omega) = \frac{1}{K_t}\sum_{\{r,q\}\in g_t} C^P_i(\phi_{i,r}, \phi_{i,q}, \omega) \tag{4.6.1b}$$

$$\bar{\alpha}_{E_i}(g_t, \omega) = \frac{1}{K_t}\sum_{\{r,q\}\in g_t} \alpha_{E_i}(A_{i,r}, A_{i,q}, \omega) \tag{4.6.1c}$$

$$\bar{\beta}_{E_i}(g_t, \omega) = \frac{1}{K_t}\sum_{\{r,q\}\in g_t} \beta_{E_i}(\phi_{i,r} - \phi_{i,q}, \omega). \tag{4.6.1d}$$

Note that we have now explicitly written the dependencies on $\omega$. Here $K_t$ is the number of receiver-pairs within each group. Thus we can evaluate the homogeneous plane-wave assumption as a function of receiver-spacing by plotting equations 4.6.1a - 4.6.1d for all the different groups $g_t = g_1, g_2, ...., g_M$. In our analysis we are not concerned with the subsurface, but it may influence our approximations. Binning receiver-pairs with respect to the distance between receivers can create some geometric dependencies. The group with the smallest receiver-spacing $\delta_{min}$ will consist of pairs scattered across the survey, while the group with the largest

receivers-spacing $\delta_{max}$ will consist of receivers closer to the rim of each survey. This can affect the approximation of the up-down going fields, if the subsurface response differs significantly from the rim to the center of the survey. However if the subsurface is homogeneous and with simple bathymetry, this effect can be neglected. In addition the number of pairs with small receiver-spacing will be considerable higher than for pairs with large spacings. Thus there is expected to be a higher uncertainty related to the pairs with large spacings.

# Chapter 5

# Results

In our analysis we consider two surveys outside the Norwegian Coast. The data stem from EMGS' multi-client library within the North Sea and Barents Sea. The approximative locations are depicted in the picture below.


Figure 5.1: Map of the EMGS multi-client library - (1) North Sea (geomagnetic latitude $\sim 60°$), (2) Barents Sea (geomagnetic latitude $\sim 110°$).

## 5.1 Two Case Studies

### 5.1.1 North Sea

Both surveys were primary CSEM surveys, however we retrieved an substantial amount of MT data when the active source was offline. For the North Sea survey we obtained 5.8 days with MT data from 59 receivers. The frequencies chosen were; 0.2604 Hz, 0.1803 Hz, 0.0651 Hz, 0.0077 Hz and 0.0044 Hz. Receiver layout is shown in Figure 5.2a and the receiver-pair spacing-distribution is plotted as a histogram in Figure 5.2b. The minimum and maximum receiver spacings are approximately 3.0 and 50.0 km. The average receiver burial depth is 350 m, with a maximum deviation of 6.0 m.

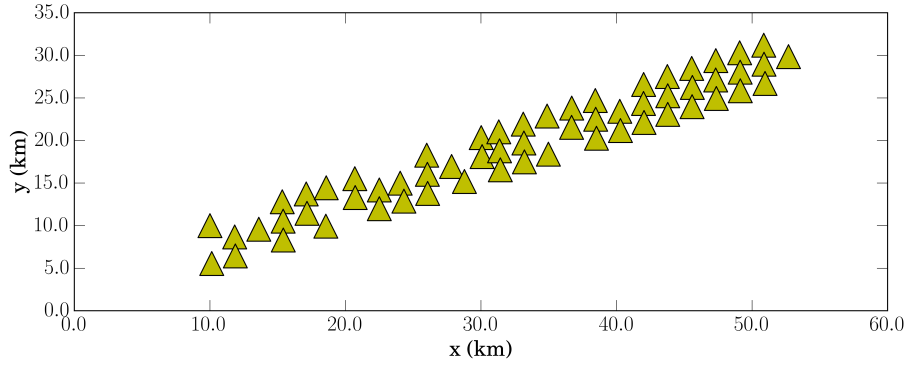


(a)

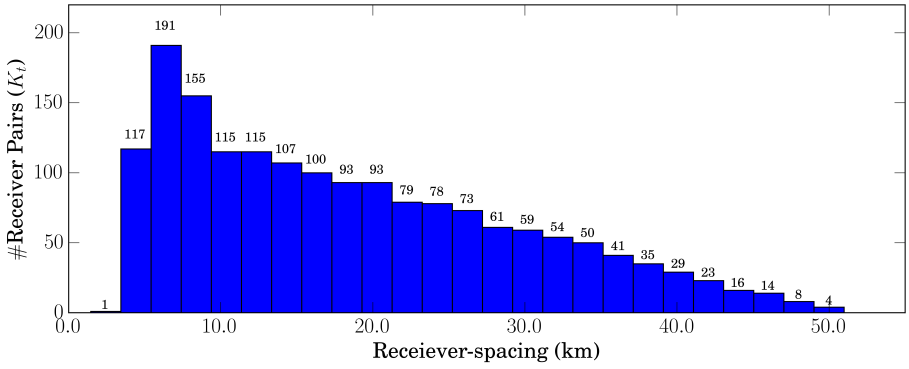


(b)

Figure 5.2: North Sea survey layout (a) and receiver-spacing distribution (b). Each bar corresponds to a group $g_t$ and the associated receiver-spacing $\delta_t$ is read of the x-axis below the bar. The bin-width is approximately 2.0 km.

### 5.1.2 Barents Sea

The Barents Sea survey contained 6.1 days of MT data taken from 50 receivers. We consider the following frequencies; 0.7210 Hz, 0.2604 Hz, 0.091 Hz, 0.023 Hz, 0.0077 Hz and 0.0044 Hz. Receiver layout is shown in Figure 5.3a and the receiver-pair spacing-distribution is plotted as a histogram in Figure 5.3b. The receivers were placed at approximately 400 m water-depth with a maximum deviation of 40 m. The receiver pair spacings stretches from 3.0 - 30.0 km.

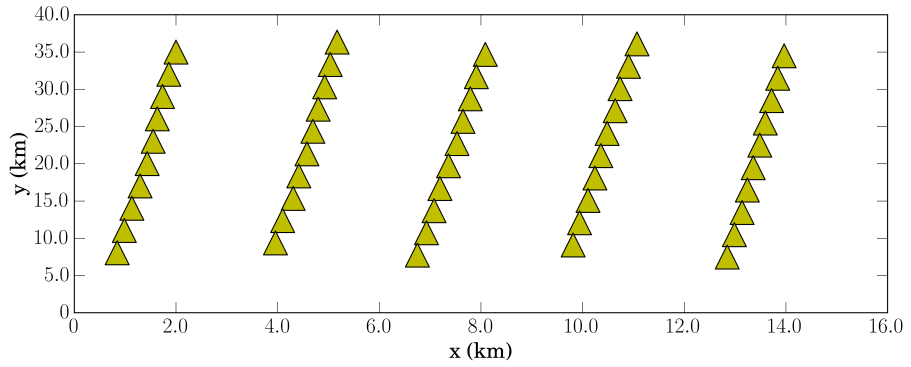


(a)

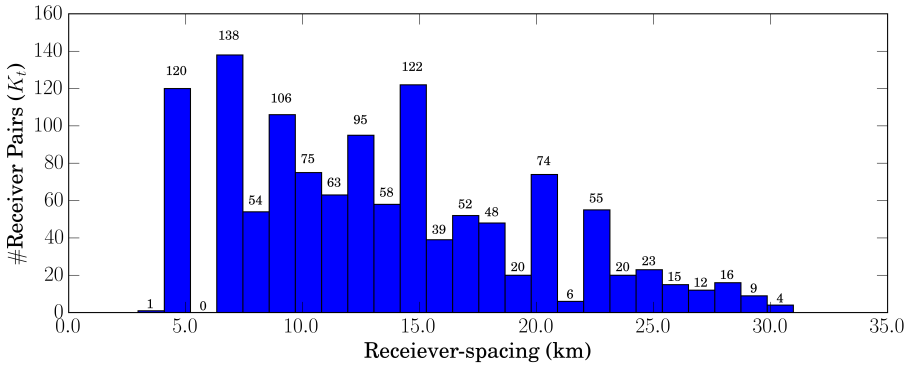


(b)

Figure 5.3: Barents Sea survey layout (xy-plane). (a) and receiver-spacing distribution (b). Each bar corresponds to a group $g_t$ and the associated receiver-spacing $\delta_t$ is read of the x-axis below the bar. The bin-width is approximately 1.1 km.

## 5.2 North Sea

### 5.2.1 Amplitude Correlation

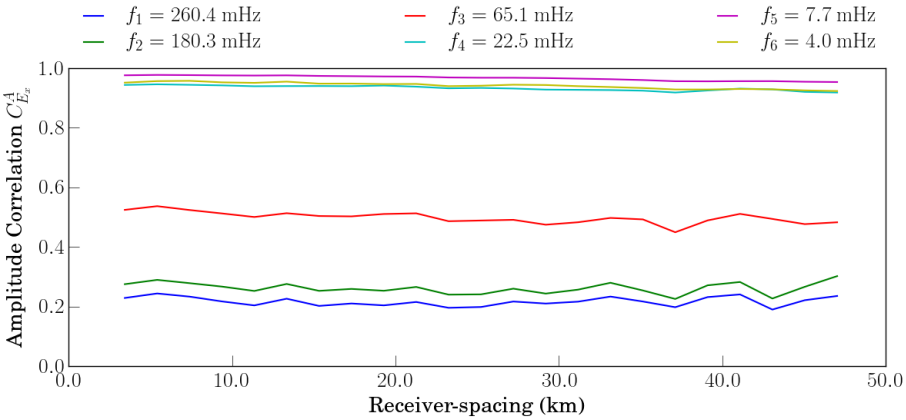


(a) Unscreened $E_x$

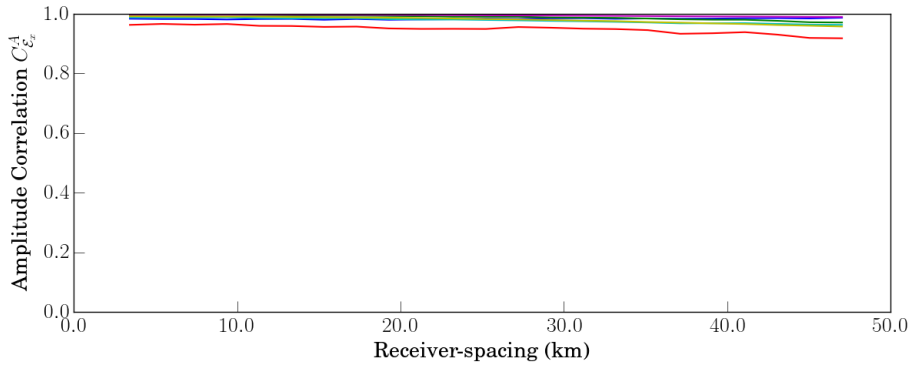


(b) Screened $\mathcal{E}_x$

Figure 5.4: Amplitude correlation factors of the approximated direct source field ($E_x$) averaged between grouped receiver-pairs from the North Sea Survey.

Applying the average amplitude correlation in equation 4.6.1a to the unscreened $E_x$ amplitude from receivers in the North-Sea survey yields both high and low degrees of correlation depending on frequency (Figure 5.4a). The low frequencies ($f_4$ - $f_6$) have correlation factors above 0.9, while the high frequencies ($f_1$ - $f_3$) are valued below 0.6. After screening, all correlation factors have converged towards unity (Figure 5.4b). There are no apparent trends in either suggesting that the degree of amplitude correlation is dependent on receiver-spacing.

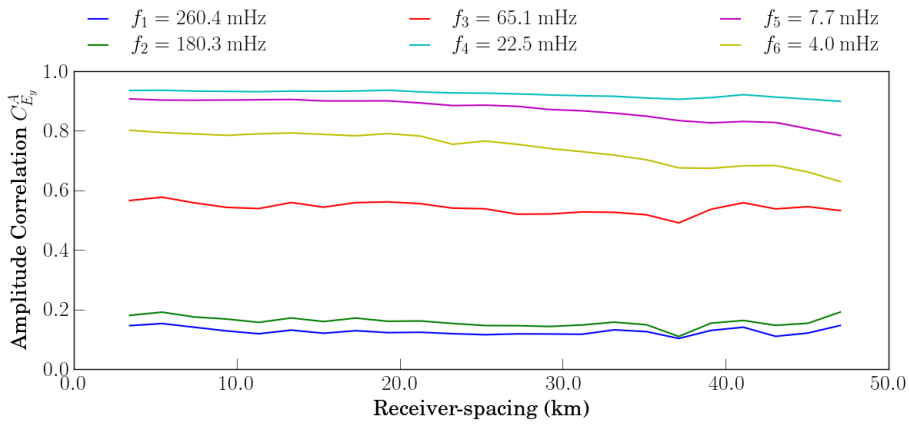


(a) Unscreened $E_x$

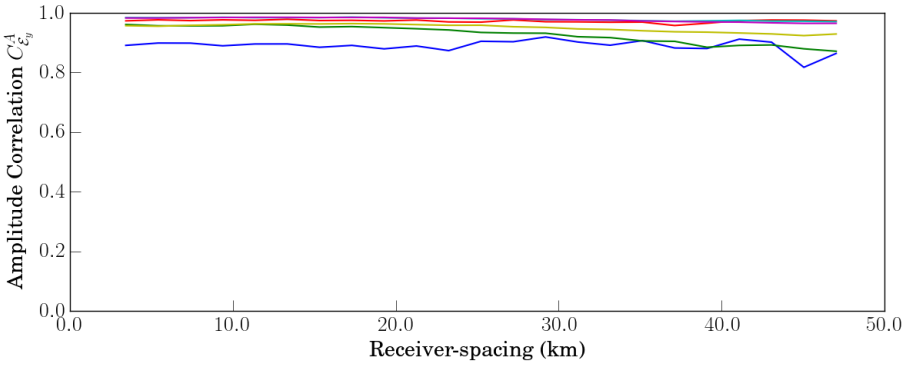


(b) Screened $\mathcal{E}_x$

Figure 5.5: Amplitude correlation factors of the approximated direct source field averaged between grouped receiver-pairs from the North Sea Survey.

Figure 5.5a show that the unscreened $E_y$ amplitude have correlation factors in the range 0.2 - 0.9 depending on frequency. High-frequency curves ($f_1$ - $f_2$) show little correlation ($< 0.2$), while the lower frequency have correlation factors between 0.6 - 0.9. After screening, amplitude correlation curves increase towards unity for all frequencies. The screened correlation factors show a weak decreasing trend. There are some differences in the amplitude correlation curves when comparing $E_x$ and $E_y$. After screening, the $\mathcal{E}_x$ amplitude correlation curves are closer to unity compared to the $\mathcal{E}_y$ amplitude correlation curves. The $f_6$ amplitude correlation curve are valued at 0.9 in the unscreened $E_x$ (Figure 5.4a) and 0.8 in the unscreened $E_y$ (Figure 5.5a). Overall the results for the averaged amplitude correlation in both unscreened and screened field components are similar for the North Sea Survey.

### 5.2.2 Phase Correlation

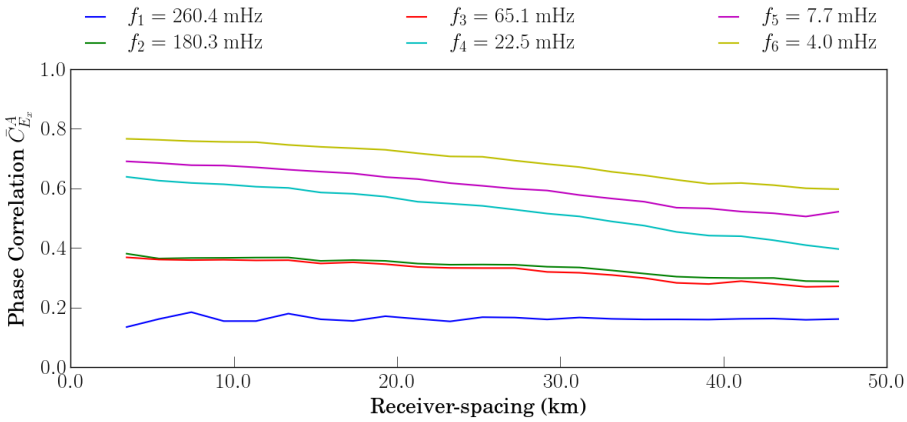


(a) Unscreened $E_x$

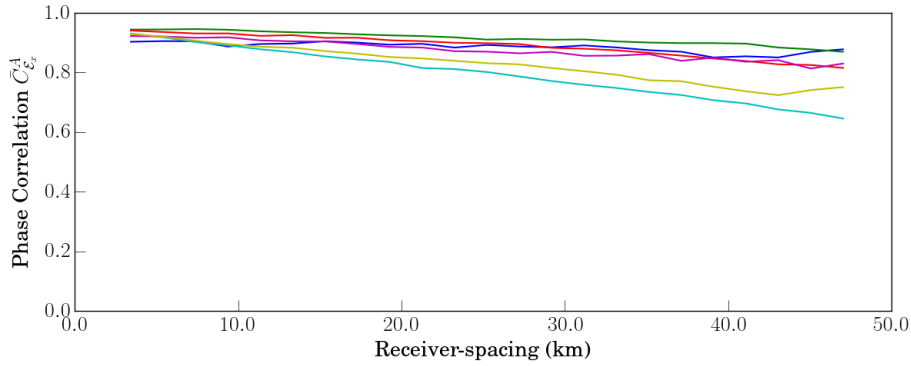


(b) Screened $\mathcal{E}_x$

Figure 5.6: Phase correlation factors of the approximated direct electric source field averaged between grouped receiver-pairs from the North Sea Survey.

The degree of correlation in unscreened electric $E_x$ phase between the North Sea receivers is between 0.2 - 0.8, depending on frequency and receiver-spacing (Figure 5.6a). High frequency curves have correlation factors below 0.4 and the lower frequency curves are valued between 0.5 - 0.8. The low frequency phase-correlation curves demonstrate a decrease in correlation factors as a function of receiver-spacing. After screening, the correlation factors increases to approximately to 0.8 - 0.9 for all frequencies (Figure 5.6b). As receiver-pair spacings increases, the degree of correlation decreases at different rates for the different frequencies for both unscreened and screened data (Figure 5.6a - 5.6b).

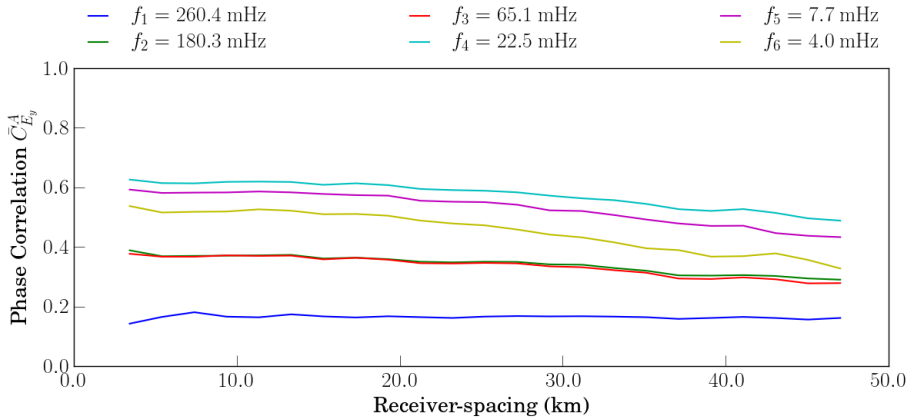


(a) Unscreened $E_x$

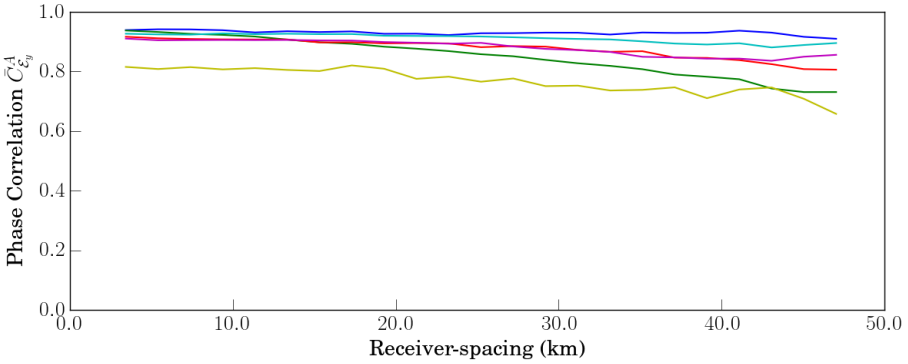


(b) Screened $\mathcal{E}_x$

Figure 5.7: Phase correlation factors of the approximated direct electric source field averaged between grouped receiver-pairs from the North Sea Survey.

Figure 5.7a demonstrates that the $E_y$ phase correlation on unscreened Northern Sea receiver data depends on frequency. High frequencies curves have correlation factors in the range 0.2 - 0.4, while low frequencies have correlation factors between 0.5 - 0.8. Screening the data in Figure 5.7b increases correlation factors for all frequencies to approximately 0.75 - 0.9. The highest frequency curve, $f_6$, have the lowest degree of correlation ($\sim 0.8$). The screened $\bar{\mathcal{C}}^P_{\mathcal{E}_y}$-curves decreases at different rates for the different frequencies. This suggest a receiver-pair spacing dependency. There are some differences when comparing unscreened phase correlation curves in $E_x$ and $E_y$. In Figure 5.6a we have $\bar{\mathcal{C}}^P_{E_x}(f_6, f_5) \sim 0.6 - 0.8$ while in Figure 5.7a we have $\bar{\mathcal{C}}^P_{E_y}(f_6, f_5) \sim 0.4 - 0.6$. Also the $f_6$ frequency correlates weaker in $\mathcal{E}_y$

compared to $\mathcal{E}_x$.

### 5.2.3 Amplitude Ratio

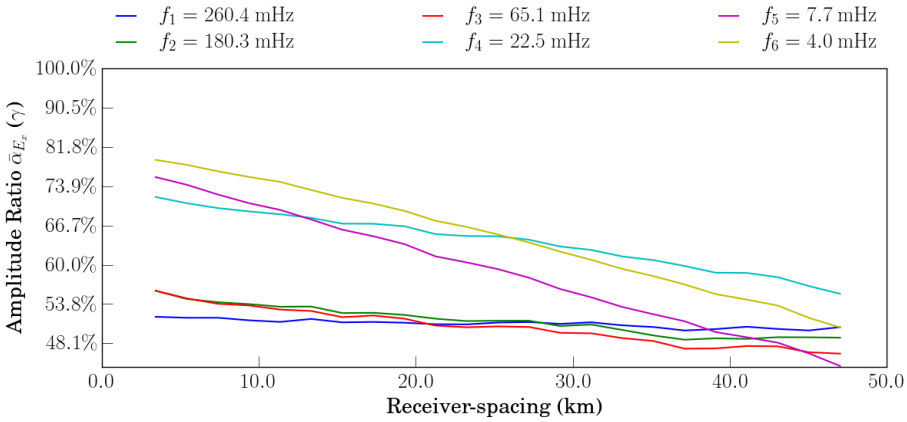


(a) Unscreened $E_x$

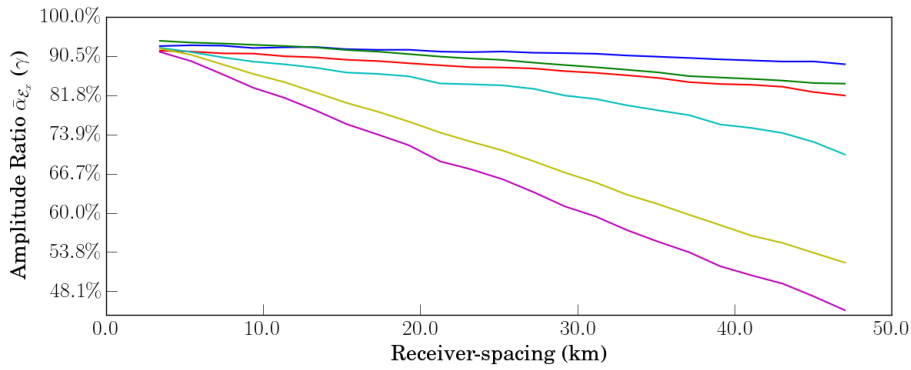


(b) Screened $\mathcal{E}_x$

Figure 5.8: Amplitude ratio of the approximated direct electric source field averaged between grouped receiver-pairs from the North Sea Survey.

Figure 5.8a demonstrate that the degree of amplitude homogeneity in $E_x$ depends on frequency. For high frequencies average amplitude ratio $\bar{\alpha}_{Ex}$is approximately $\sim 50\%$. For lower frequencies, the average amplitude ratio start at $\sim 70\%$ and drop to 50 % as receiver-spacing increases. The curves $\bar{\alpha}_{E_x}(f_5)$ and $\bar{\alpha}_{E_x}(f_6)$ demonstrate a steep negative slope, decreasing a total of 30 percentage points. The other frequencies only decrease 3-5 % for equivalent spacings. After screening, Figure 5.8b show that $\bar{\alpha}_{\mathcal{E}_x}$ increases in fitness-percentages for all frequencies. Each screened

$\bar{\alpha}_{\mathcal{E}_x}$-curve show a decreasing trend as a function of receiver-spacing. The two low frequency curves, $\bar{\alpha}_{\mathcal{E}_x}(f_5)$ and $\bar{\alpha}_{\mathcal{E}_x}(f_6)$ stands out with a high negative slope, decreasing in 40%-percentage points in fitness value as receiver-spacing increases.

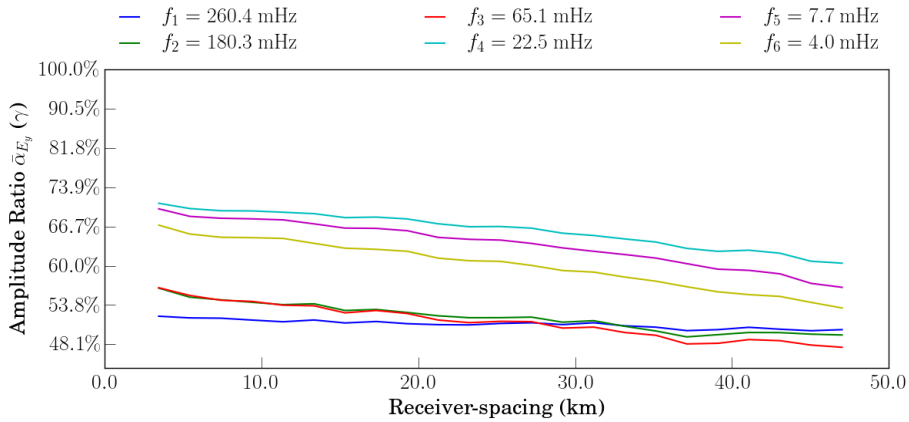


(a) Uncreened $E_y$

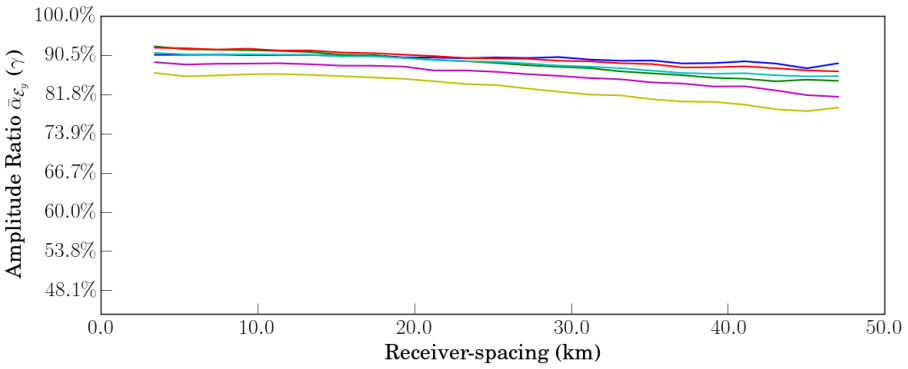


(b) Screened $\mathcal{E}_y$

Figure 5.9: Amplitude ratio of the approximated direct electric source field averaged between grouped receiver-pairs from the North Sea Survey.

The unscreened amplitude ratio $\bar{\alpha}_{E_y}$-curves in Figure 5.9a are separated by the low ($f_4$ - $f_6$) and high ($f_1$ - $f_3$) frequencies. The low frequency $\bar{\alpha}_{E_y}$-curves start at $\simeq$ 67% and then decreases to 60%. The higher frequency curves are valued at approximately between 55% and 49%, decreasing as receiver-spacing increases. After screening, all amplitude ratio curves increase toward $\sim$ 90% (Figure 5.9b). Both $\bar{\alpha}_{E_x}$ and $\bar{\alpha}_{E_y}$ amplitude show comparable trends with fitness-percentages as a function of receiver-spacing, except for the two highest frequency curves.

### 5.2.4 Associated Phase Difference

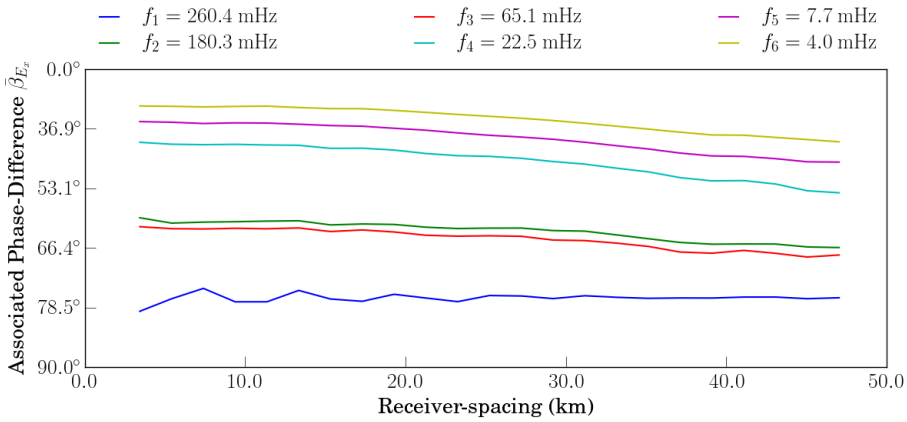


(a) Unscreened

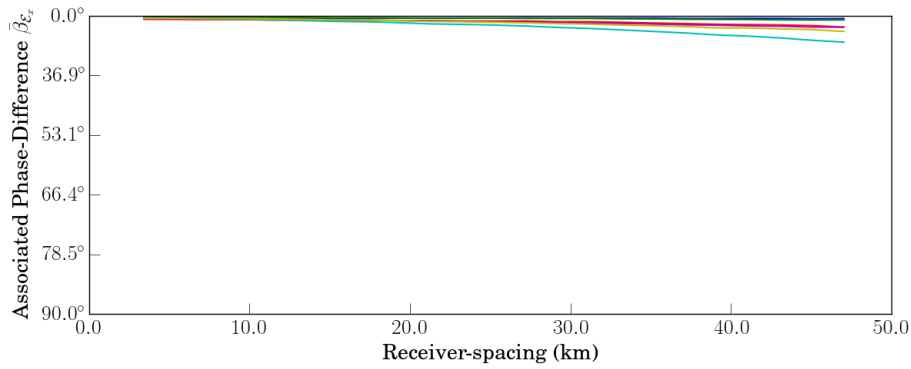


(b) Screened

Figure 5.10: Associated phase-differences of the approximated direct source field ($E_x$) averaged between grouped receiver-pairs from the North Sea Survey.

The unscreened associated phase-differences $\bar{\beta}_{E_x}$ averaged between receiver-pairs of the North Sea Survey shown in Figure 5.10a display a frequency dependency. High frequency curves, $f_1$ - $f_3$, have a $\bar{\beta}_{E_x}$ values corresponding to an phase-difference between 60 - 80°. Lower frequency curves are valued between 26 - 53° in phase-differences. All the $\bar{\beta}_{E_x}$-curves, except $\bar{\beta}_{E_x}(f_1)$, show a negative linear trend with respect to receiver spacing. The screened $\bar{\beta}_{\mathcal{E}_x}$-curves converges towards zero for all frequencies (Figure 5.10b). However, as receiver-spacings increases, the $\bar{\beta}_{\mathcal{E}_x}$-curves tend to separate. At approximately 45.0 km $\bar{\beta}_{\mathcal{E}_x}(f_4)$ decreases in fitness to approximately 20° phase-difference.

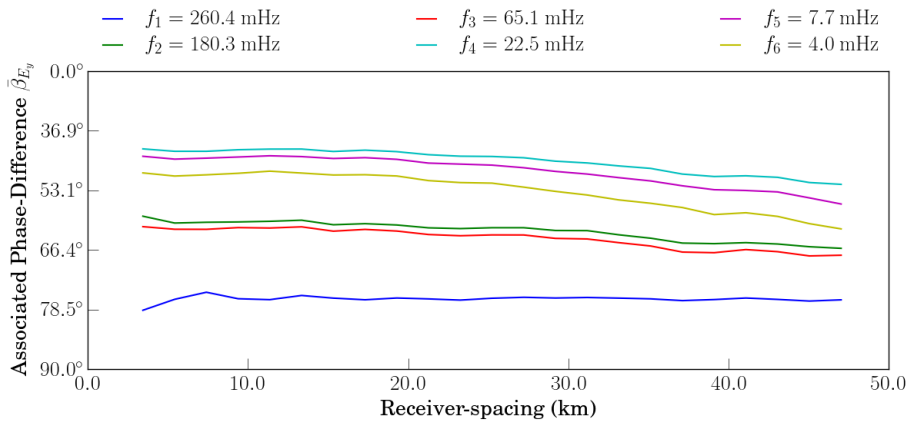


(a) Unscreened

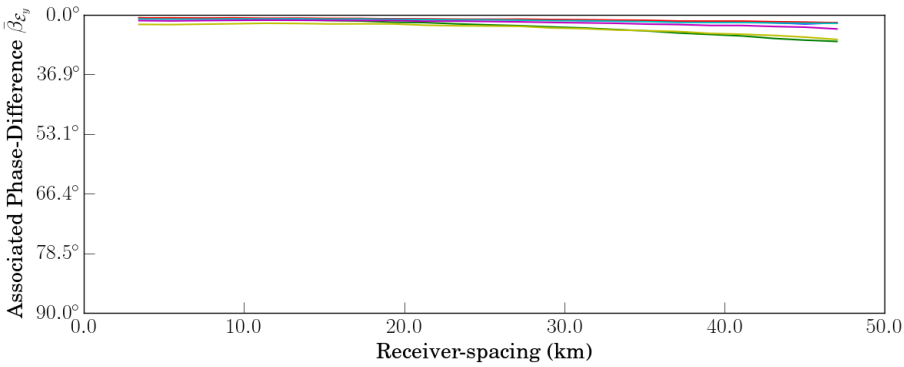


(b) Screened

Figure 5.11: Associated phase-differences of the approximated direct source field ($E_y$) averaged between grouped receiver-pairs from the North Sea Survey.

The results in Figure 5.11a show that the associated phase-difference $\beta_{E_y}$ between receiver-pairs in the North Sea is frequency dependent. High frequency $\beta_{E_y}$-curves are valued between $60.0° - 75°$ degrees, and the lower frequencies are centred around $40.0° - 55°$-degrees. Every curve, except $\beta_{E_y}(f_1)$, show a decreasing trend with respect to receiver-pair spacing. The high frequency $\beta_{E_y}(f_1)$-curve is valued approximately at 76° degrees for all receiver-spacings. After screening the $\beta_{\mathcal{E}_y}$-curves converge to zero. There is a weak trend showing that the $\beta_{\mathcal{E}_y}$-curves depends on receiver-spacing.

## 5.3 Barents Sea

### 5.3.1 Amplitude Correlation

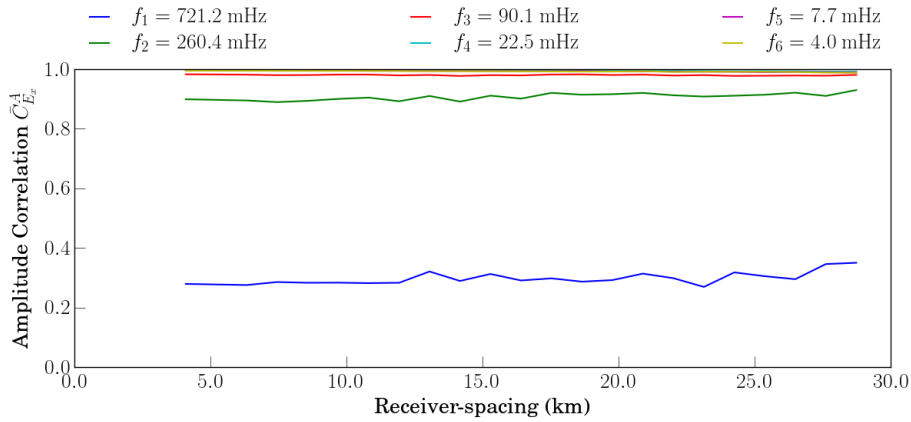


(a) Unscreened $E_x$

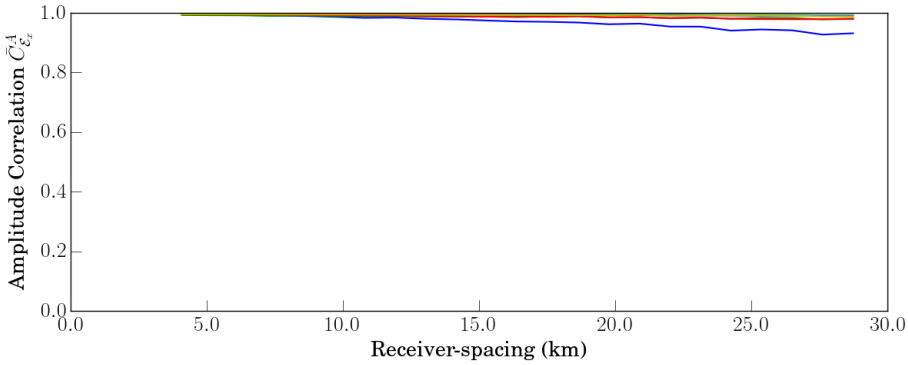


(b) Screened $\mathcal{E}_x$

Figure 5.12: Amplitude correlation factors of the approximated direct source field ($E_x$) averaged between grouped receiver-pairs from the Barents Sea Survey.

The average $E_x$ amplitude correlation factors of the Barents Sea survey show a high degree of correlation ($> 0.9$) between all receiver-pairs and frequencies, except for frequency $f_1$ which is valued at $\sim 0.3$ (Figure 5.12a). The screened amplitude correlation curves in Figure 5.12b have all converged towards unity. There is a weak trend suggesting that $\bar{\mathcal{C}}^A_{\mathcal{E}_x}(f_1)$ decreases as a function of receiver-spacing. The other frequencies however does not show this trend.

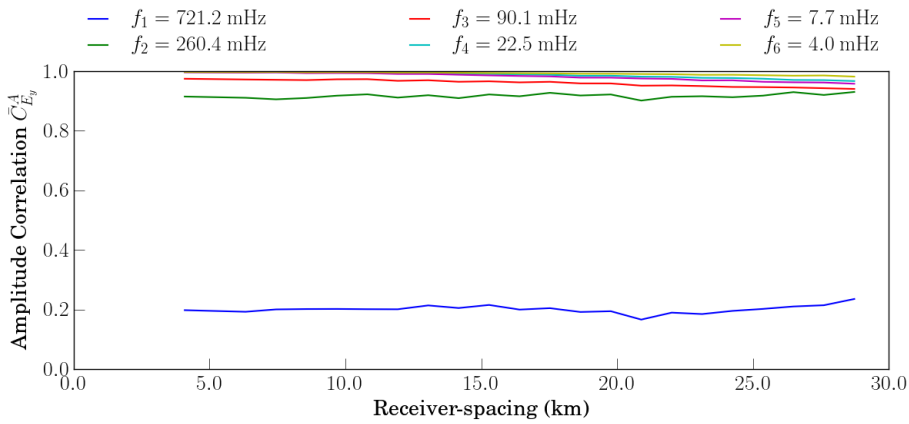


(a) Unscreened $E_y$

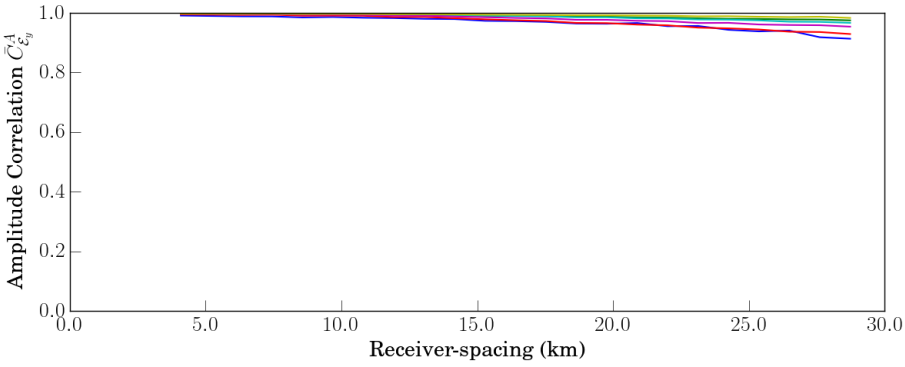


(b) Screened $\mathcal{E}_y$

Figure 5.13: Amplitude correlation factors of the approximated direct source field ($E_y$) averaged between grouped receiver-pairs from the Barents Sea Survey.

The average $E_y$ amplitude correlation in Figure 5.13a have correlation factors above 0.9, except for the highest frequency curve, which have a correlation factor of 0.2. After screening, all $\bar{C}^A_{\mathcal{E}_y}$-curves converges towards unity (Figure 5.13b). For receiver-spacings above 25.0 km, the screened amplitude correlation factors tend to decrease. Overall, amplitude correlation factors for the Barents Sea survey are similar in both field components.

### 5.3.2 Phase Correlation

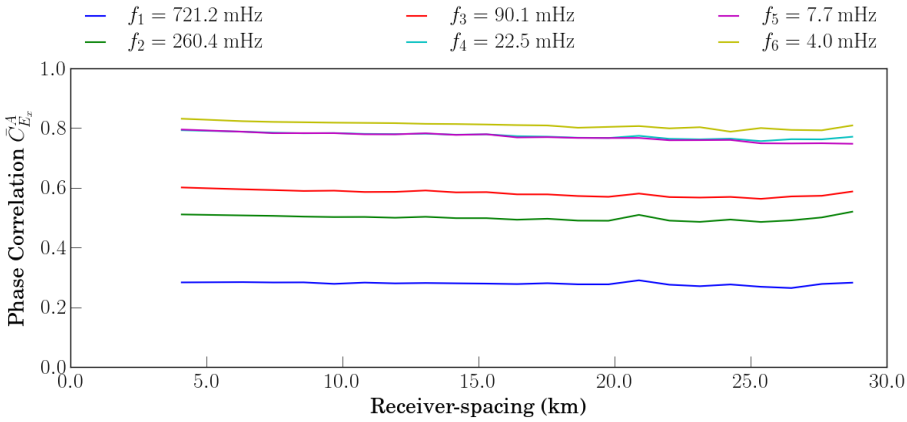


(a) Unscreened $E_x$

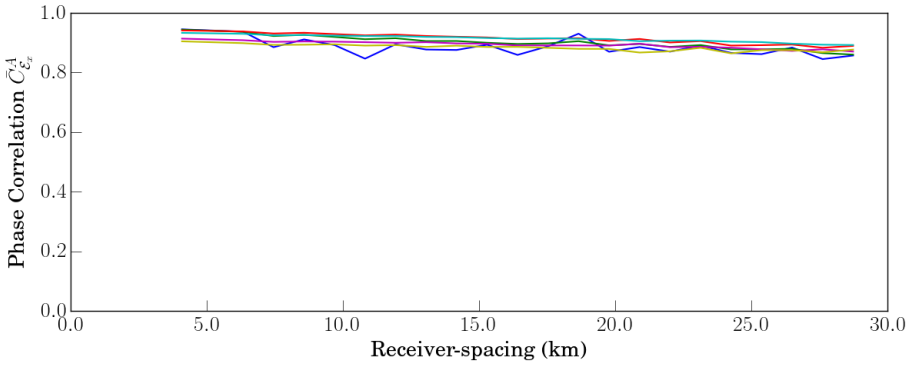


(b) Screened $\mathcal{E}_x$

Figure 5.14: Phase correlation factors of the approximated direct source field ($E_x$) averaged between grouped receiver-pairs from the Barents Sea Survey.

Figure 5.14a demonstrate that average $E_x$ phase correlation factors for the Barents Sea data depends on frequency. The phase correlation factors vary between 0.3 - 0.8 for the respectively high and low frequencies. Screening the data increases the correlation-curves to approximately 0.9 (Figure 5.14b). There is a weak decreasing trend for the screened phase-correlation factors.

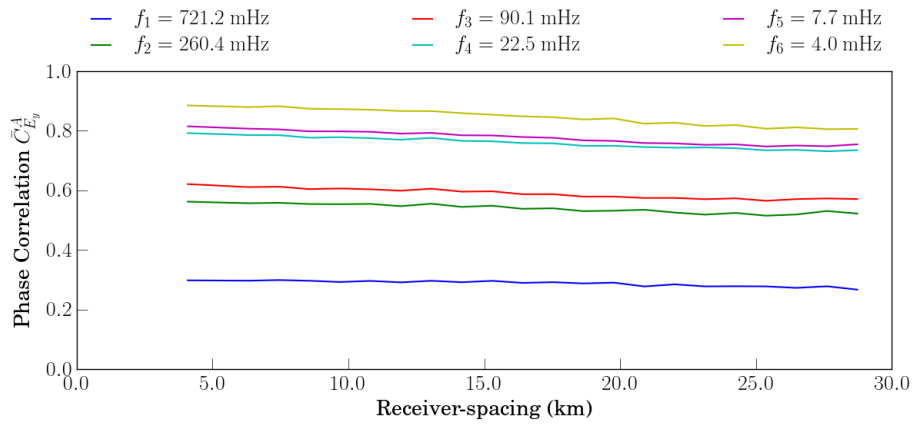


(a) Unscreened $E_y$

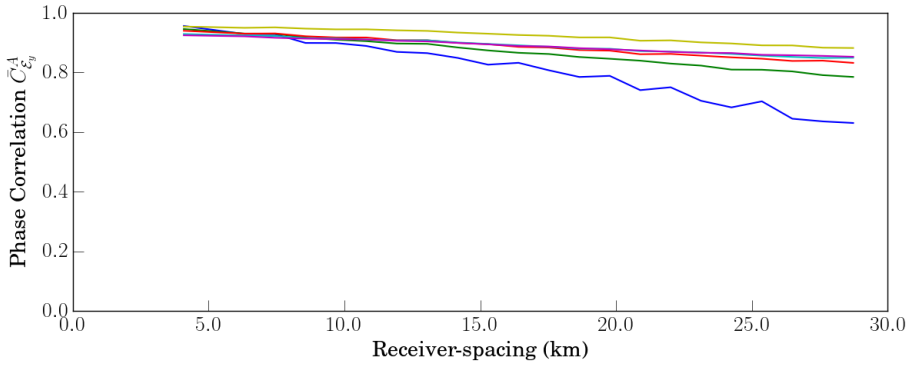


(b) Screened $\mathcal{E}_y$

Figure 5.15: Phase correlation factors of the approximated direct source field ($E_y$) averaged between grouped receiver-pairs from the Barents Sea Survey.

The average correlation factors of the unscreened $E_y$ phase in Figure 5.15a show that the receiver-pairs correlate at different degrees as a function of frequency. The high frequency data have correlation factors between 0.3 - 0.6, while the lower frequencies are valued at approximately 0.8. There is a weak trend suggesting that the screened $\bar{\mathcal{C}}^P_{\mathcal{E}_y}$ depends on the receiver-spacing (Figure 5.15b). The correlation factors for all frequencies have increased to approximately 0.9 (Figure 5.15b), except for $\bar{\mathcal{C}}^P_{\mathcal{E}_y}(f_1)$ which decrease to 0.8 for large receiver-spacings. The results for averaged phase-correlation between receiver-pairs show equivalent results in both field components.

### 5.3.3 Amplitude Ratio

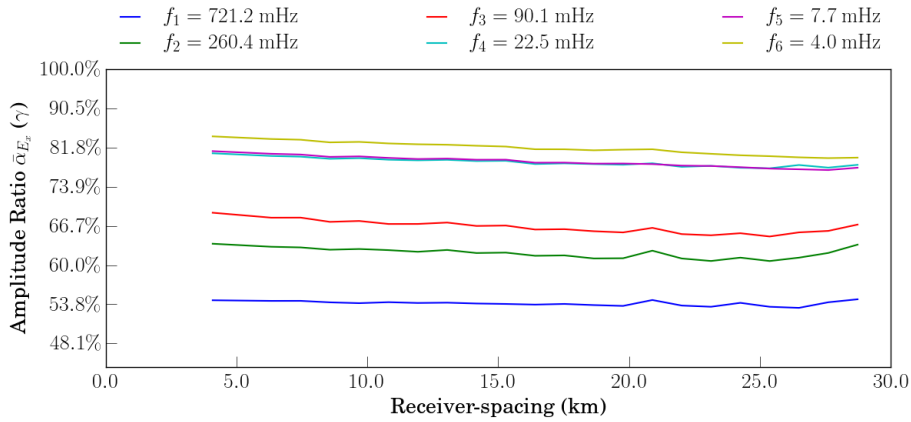


(a) Unscreened $E_x$

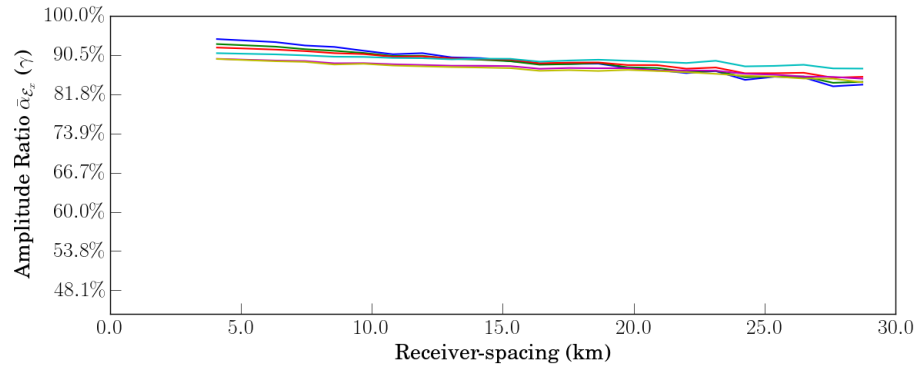


(b) Screened $\mathcal{E}_x$

Figure 5.16: Amplitude ratio of the approximated direct source field ($E_x$) averaged between grouped receiver-pairs from the Barents Sea Survey.

Figure 5.16a show that the average amplitude ratio $\alpha_{E_x}$ depends on frequency. The higher frequency curves have $\alpha_{E_x}$-values $\sim 80.0\%$, while lower frequency curves are valued between $53\% - 67\%$. The average amplitude ratio show little variations with respect to receiver-spacing. After screening we observe that the $\alpha_{\mathcal{E}_x}$-curves have increased to $85 - 92\%$ for all frequencies(Figure 5.16b). There is some decreasing trends for $\alpha_{\mathcal{E}_x}$ as a function of receiver-spacing, but it is not apparent how this relates to the frequency.

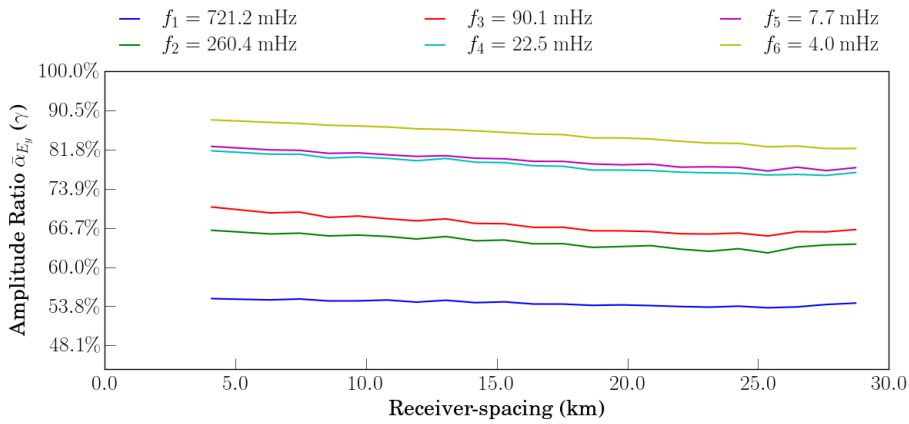


(a) Unscreened $E_x$

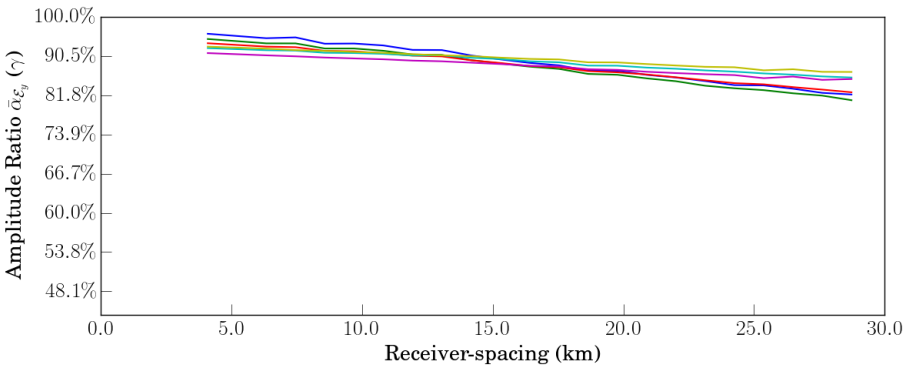


(b) Screened $\mathcal{E}_x$

Figure 5.17: Amplitude ratio of the approximated direct source field ($E_y$) averaged between grouped receiver-pairs from the Barents Sea Survey.

Figure 5.17a show that $\bar{\alpha}_{E_y}$ have approximately the same degree of homogeneity and frequency-dependency as for $\alpha_{E_x}$ in Figure 5.16a. High frequency curves are valued between 53 - 70%, and low frequency curves are valued 82 - 90% in homogeneity. There is a weak decreasing trend for the low frequency $\bar{\alpha}_{E_y}$ in Figure 5.17a. After screening, every amplitude ratio curve have increased to 81 - 95% (Figure 5.17b). Both unscreened and screened $E_x$ amplitude ratio show a decreasing trend as a function of receiver-spacing.

### 5.3.4 Associated Phase Difference

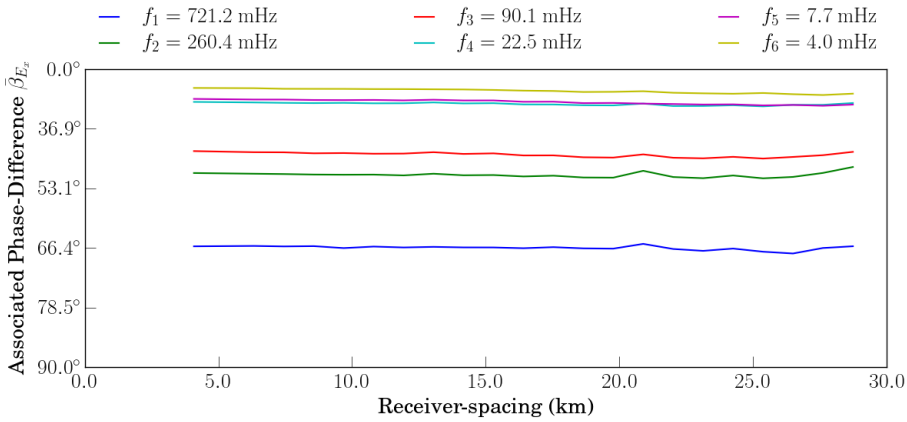


(a) Unscreened $E_x$

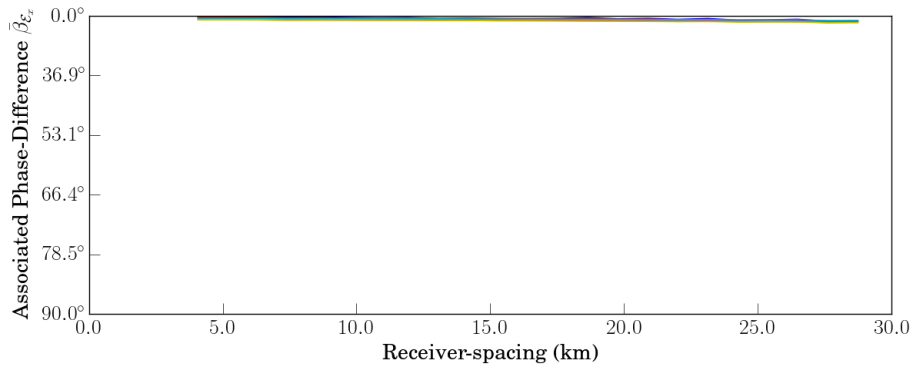


(b) Screened $\mathcal{E}_x$

Figure 5.18: Average associated phase-difference of the unscreened (a) and screened (b) redatumed down-going $E_x$ field component obtained in the Barents Sea survey.

In Figure 5.18a, we see that unscreened $E_x$ associated phase-differences between receiver-pairs in the Barents Sea survey is dependent on frequency. The magnitude of the $\bar{beta}_{E_x}$-curves, ranging from lowest to highest frequency are valued between $10° - 70°$, respectively. After screening we observe that the average associated phase-difference have converged towards zero for all frequencies (Figure 5.18b). There are no apparent trends showing a receiver-spacing dependency in either unscreened or screened $E_x$ data.

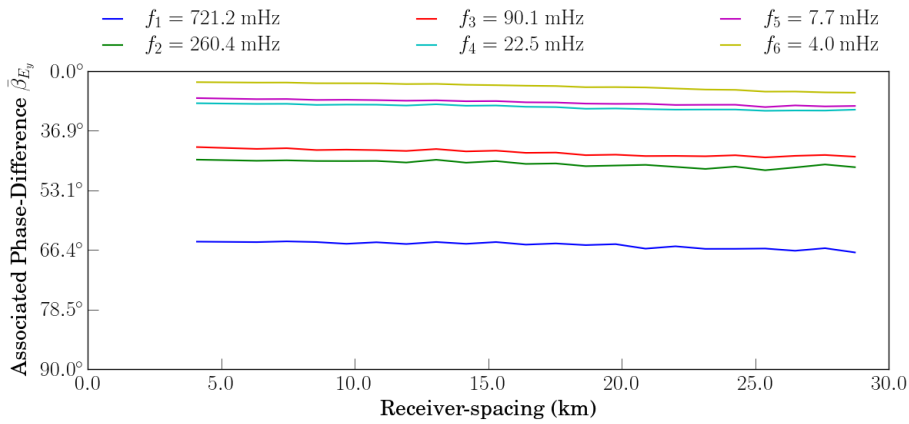


(a) Unscreened $E_x$

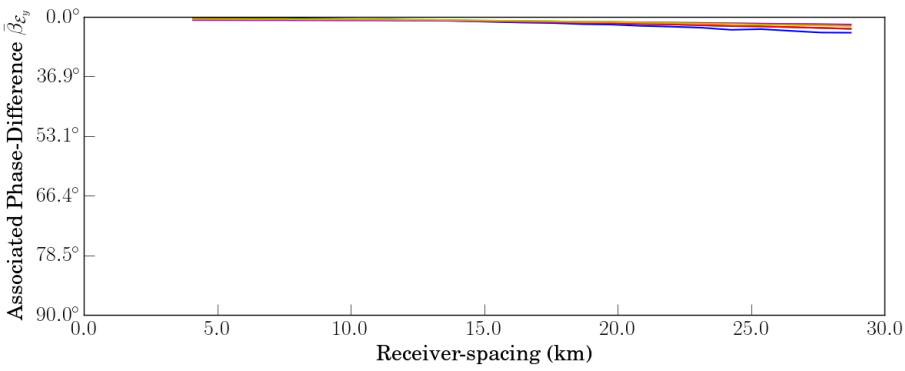


(b) Screened $\mathcal{E}_x$

Figure 5.19: Average associated phase-difference of the unscreened (a) and screened (b) redatumed down-going $E_y$ field component obtained in the Barents Sea survey.

Figure 5.17a shows that the associated phase-difference $\beta_{E_y}$ is dependent on frequency. Low frequency $\beta_{E_y}$-curves are valued between $5° - 20°$, while the higher frequencies are between $40° - 66°$. The screened average associated phase-difference in Figure 5.19b have converged toward zero. There is a weak trend suggesting an increase in phase-differences for increasing receiver-spacings. The associated phase-differences behave equivalently with respect to frequency and receiver-spacing in both field components.

## 5.4 General Observations

### 5.4.1 Screening Effects

The most striking (and unexpected) result is how screening impacts our results. Screening increases amplitude- and phase-correlation, and decreases the scaled residuals of amplitude ratio and associated phase-differences between receivers. The high frequency data contain more noise and non-physical measurements and thus experience a larger screening effect. As frequency is lowered, the screening contributions from the noise-filters reduces to zero while the Q-ratio and Poynting criteria screens roughly 0 - 20 % per receiver in the North Sea survey and 0 - 8 % per receiver in the Barents Sea survey. The limits in Q-ratio and Poynting test (equations 4.1.5 - 4.1.7) could be softened with an appropriate noise term. To test whether the screened events are local (between closest receivers) or if they are global (entire survey) we correlated the associated Q-,S-screening times between all receivers. The results showed very little correlation ($\sim 0.1 - 0.2$). Therefore we suspect that the high frequency screening contributions most likely stem from local receiver effects, such as motional disturbances of the receivers as discussed in chapter 3.1. However, for the lower frequencies the screening may stem from non-uniform source events.

### 5.4.2 Amplitude- and Phase relations

The screened amplitude- and phase-correlation factors were found to be in the range $0.7 - 1.0$ in both surveys. The amplitude-correlation factors were in general higher compared to the phase-correlation factors. This might come from wrapping effects in the phase. However, we do emphasize that the estimated correlation factors may be below their true value due to outliers and noise. Both amplitude and phase showed a decrease in correlation factors as the receiver-spacing increases. A high correlation in amplitude and phase is expected for homogeneous plane-wave model.

There were some discrepancy in the amplitude ratio test for the North Sea survey (Figures 5.8a - 5.8b), where the lowest frequency curves had a significant steep downhill slope. The fact that the corresponding frequencies, had high amplitude correlation factors ($\sim 1.0$), suggest an influence of a coherent signal. It may be the active CSEM source, sending fields into the subsurface which in turn is guided to the receivers. It could also be a significant inhomogeneous event from the ionospheric source. Further analysis is required to determine these anomalies. We do note that these effects were not observed in the other North Sea survey which were conducted at a different time. The other amplitude ratio curves behaved consistent, and were valued between $80 - 95\%$ in both surveys. In general the amplitude ratio displayed an apparent dependency on the receiver-spacings. Homogeneity in amplitude was found to be stronger for nearest neighbouring receivers, and weaker for receivers further apart, which is consistent with the amplitude correlation factors.

The associated phase-difference demonstrated little deviation from the plane-

wave model for receiver-spacings up to approximately 30.0 km in both surveys. For larger receiver-spacings ($> 30$ km) in the North Sea survey, there is a stronger trend suggesting deviation from a plane-wave model. However this number must be interpreted with care, due to the effects of receiver-layout and corresponding receiver-spacing distributions as discussed in Chapter 4.6.

## 5.5 Closing Remarks

In this thesis we have analysed the approximated direct source field by using the down-going field obtained from up-down decomposition above the seabed. Subsequently we have quantified the deviations from the homogeneous plane-wave assumption as a function of receiver-spacing and frequency in two separate surveys. For the datasets we have considered, both amplitude and phase demonstrated an apparent dependency on receiver-spacings. The approximation works better for nearest neighbouring receivers, but showed deviations as the receiver-spacings increases. The results obtained here are consistent with two additional surveys, located in nearby regions.

## 5.6 Future Applications

As shown in this thesis, extracting the down-going field above the seabed can provide valuable source information, which in turn can be used in further MT processing schemes. The high impact of screening displayed in our results, may suggest that the raw MT data contain considerable less amount of MT than previously thought. It would be interesting to examine how the screening algorithm performs with the standard multivariate processing schemes, like the RMEV-method. Hence, the screening algorithms could serve as a quality control for noise-estimates.

# Bibliography


Amundsen, L., Løseth, L., Mittet, R., Ellingsrud, S., and Ursin, B. (2006). Decomposition of electromagnetic fields into upgoing and downgoing components. *Geophysists*, 71(5):G211 – G223.

Cagniard, L. (1953). Basic theory of the magneto-telluric method of geophysical prospecting. *Geophysics*, 18:605–635.

Carrasquilla, A. and Rijo, L. (1998). Analysis of electrojet-distorted magnetotelluric sounding curves. *Journal of Applied Physics*.

Chave, A. D. and Jones, A. G. (1987). *The Magnetotelluric Method: Theory and Practice*. Cambridge University Press.

Chave, A. D. and Lezaeta, P. (2006). The statistical distribution of magnetotelluric apparent resistivity and phase. *Geophysics*, 171:127–132. doi: 10.1111/j.1365-246X.2007.035.

Chave, A. D. and Thomson, D. J. (2004). Bounded influence magnetotelluric response function estimation. *Geohpysics*, 157:988–1006.

Chave, A. D., Thomson, D. J., and Ander, M. E. (1987). On the robust estimation of power spectra, coherences, and transfer functions. *Geophysical Research*, 92(B1):633–648.

Constable, S. (2010). Ten years of marine csem for hydrocarbon exploration. *Geophysics*, 75(5):A67–A81.

de la Kethulle de Ryhove, S. and Mittet, R. (2014). 3d marine magnetotelluric modeling and inversion with the finite-difference time-domain method. *Geophysics*, 79(6):E269–E286. doi: 10.1190/geo2014-0110.1.

Dmitriev, V. I. and Berdichevsky, M. N. (1979). The fundamental model of magnetotelluric sounding. *Proceedings of the IEEE*.

Egbert, G. D. (1997). Robust multiple-station magnetotelluric data processing. *Geohpysics*, 130:475–496.

Egbert, G. D. (2002). Processing and interpretation of electromagnetic induction array data. *Surveys in Geophysics*, 23:207–249.

Eidsmo, T., Ellingsrud, S., and and, S. J. (2002). "seabed logging:" a possible direct hydrocarbon indicator for deepsea prospects using em energy. *First Break*, 20(144-152).

Gamble., T. D., M.Goubau, W., and Clarke, J. (1979). Magnetotellurics with a remote reference. *Geophysics*, 44:53–68.

Griffiths, D. J. (2008). *Introduction To Electrodynamics*. Pearson, 3. edition.

Hermance, J. (1978). Electromagnetic induction in the earth by moving ionospheric current systems. *Geophysics*.

Hermance, J. F. and Peltier, W. R. (1970). Magnetotelluric fields of a line current. *American Geophysical Union*.

Hibbs, R. D. and Jones, F. W. (1976a). The calculation of the electromagnetic fields of a sheet current source with arbitrary spatial intensity distribution over a layered half space - part 1 general methods and results. *Geophysics*.

Hibbs, R. D. and Jones, F. W. (1976b). The calculation of the electromagnetic fields of a sheet current source with arbitrary spatial intensity distribution over a layered half space - part 2 the computer program and it's applications. *Geophysics*.

Hohmann, G. W. and Raiche, A. P. (1988). Inversion of controlled-source electromagnetic data. *Earth and Planetary Sciences*, 8:468 – 504. DOI:10.1190/1.9781560802631.ch8.

Hoversten, G. M., Constable, S. C., and Morrison, H. F. (2000). Marine magnetotellurics for base-of-salt mapping:gulf of mexico field test at the gemini structure. *Geophysics*, 65(5):1476–1488.

Jones, A. G., Chave, A. D., Egbert, G., Auld, D., and Bahr, K. (1989). A comparison of techniques for magnetotelluric response function estimation. *Journal of Geophysical Research*, 94(10):14201 – 14214.

Jones, A. G. and Spratt, J. (2002). A simple method for deriving the uniform field mt responses in auroral zones. *Earth Planets Spaces*, pages 443–450.

Key, K. and Constable, S. (2010). Coast effect distortion of marin magnetotelluric data: Insights from a pilot study offshore northeastern japan. *Physics of the Earth and Planetary Interiors*.

Key, K. W., Constable, S. C., and Weiss, C. J. (2006). Mapping 3d salt using the 2d marine magnetotelluric method: Case study from gemini prospect, gulf of mexico. *Society of Exploration Geophysics*, 71(1):B17– B27. DOI:10.1190/1.2168007.

Kievelson, M. G. and Russel, C. T. (1995). *Introduction to Space Physics*. Cambridge University Press.

Kumar, K., Borgohain, D., Morten, J. P., Mrope, F., Panzner, M., and Kumar, D. (2014). Offshore sub-basalt exploration using csem and mt. *Geophysics*, 24.

Lezaeta, P. F., D.Chave, A., and Evans, R. L. (2005). Correction of shallow-water electromagnetic datafor noise induced by instrument motion. *Geophysics*, 70(5):G127–G133. doi:10.1190/1.2080748.

MacGregor, L. (2003). Joint analysis of marine active and passive source em data for sub-salt and sub-baslt imaging. *65th EAGE Conference and Exhibition*.

Madden, T. and Nelson, P. (1964). A defense of cagniard's magnetotelluric method. *Geophysics*.

Mareschal, M. (1986). Modelling of natural sources of magnetospheric origin in the interpretation of regional induction studies: A review. *Surveys in Geophysics*.

Mittet, R. and Gabrielsen, P. T. (2013). Decomposition in upgoing and downgoing fields and inversion of marine csem data. *Geophysics*, 78(1):17.

Mittet, R. and Morten, J. P. (2012). Detection and imaging sensitivity of the marine csem method. *Geophysics*, 77(6):E411–E425. DOI:10.1190/geo2012-0016.1.

Nordskag, J. I. and Amundsen, L. (2007). Asymptotic airwave modeling for marine controlled-source electromagnetic surveying. *Geophysics*, 72(6):F249–F255. doi: 10.1190/1.2786025.

Ollila, E., Tyler, D. E., and Poor, H. V. (2012). Complex elliptically symmetric distributions:survey, new results and applications. *IEEE Transactions on Signal Processing*.

Osipova, I. L., Hjelt, S. E., and Vanyan, L. (1989). Source field problems in the northern parts of the baltic shield. *Physics of Earth and Planetary Interiors*.

Padilha, A. L. (1999). Behaviour of magnetotelluric source fields within the equatorial zone. *Earth Planets Space*.

Panzner, M., Weibeull, W. W., and Morten, J. P. (2014). Sub-basalt imaging in the faroe-shetland island using csem and mt data to constrain the velocity model. *Society of Exploration Geophysics*, 24:3806–3810. DOI:10.1190/segam2014-0715.1.

Percival, D. B. and Walden, A. T. (1993). *Spectral Analysis for Physical Applications*. Cambridge University Press.

Pirjola, R. J. (1998). Modelling the electric and magnetic fields at the earth's surface due to an auroral electrojet. *Atmospheric and Solar-Terrestrial Physics*.

Price, A. T. (1962). The theory of magnetotelluric methods when the source field is considered. *Geophysical Research*, page 1907–1918.

Prieto, G. A., Parker, R. L., Thomson, D. J., Vernon, F. L., and Graham, R. L. (2007). Reducing the bias of multitaper spectrum estimates. *Geophysics*, 171:1269–1281.

Simpson, F. and Bahr, K. (2004). *Practical Magnetotellurics*. Cambridge.

Srivastava, S. P. (1965). Method of interpretation of magnetotelluric data when source field is considered. *Geophysics*.

Thomson, D. J. (1982). Spectrum estimation and harmonic analysis. *Proceedings of the IEEE*, 70:1055–1096.

Tikhonov, A. N. (1950). The determination of the electrical properties of deep layers of the earth's crust. *Doklady*, 73:295–297.

Ursin, B. (1983). Review of elastic and electromagnetic wave propagation in horizontally layered media. *Geophysics*, 48(8):1063–1081.

Viljanen, A., Pirjola, R., and Amm, O. (1999). Magnetotelluric source effect due to 3d ionospheric current systems usingthe complex image method for 1d conductivity structures. *Earth Planets Space*.

Viljanen, A., Pirjola, R., and Hakkinen, L. (1993). An attempt to reduce induction source effects at high latitudes. *Geomagnetism and Geoelectricity*.

Vozoff, K. (1972). The magnetotelluric method in the exploration of sedimentary basins. *Geophysics*, 37:325–328.

Vozoff, K. (1991). The magnetotelluric method. *Society of Exploration Geophysist*, pages 641–712. in Misac N. Nabighian:Electromagnetic Methods in Applied Geophysics.

Wait, J. R. (1954). On the relationship between telluric currents and the earth's magnetic field. *Geophysics*, 19(2):281–289. doi: 10.1190/1.1437994.

Ward, S. H. and Hohmann, G. W. (1989). Electromagnetic theory for geophysical applications. *Society of Exploration Geophysists*, 1(3):131 – 311.

Wei, W. W. (2006). *Time Series Analysis : Univariate and Multivariate Methods (2nd Edition)*. Pearson.

Weidelt, P. (1972). The inverse problem of geomagnetic induction. *Journal of Geophysics*, B(38):257 – 289.